VORTICES IN COHERENT AND PARTIALLY COHERENT OPTICAL BEAMS

by

Charlotte Susan Dulaney Stahl

A dissertation submitted to the faculty of
The University of North Carolina at Charlotte
in partial fulfillment of the requirements
for the degree of Doctor of Philosophy in
Optical Science and Engineering

Charlotte

2018

Approved by:

_____
Dr. Gregory Gbur

_____
Dr. Michael Fiddy

_____
Dr. Angela Davies

_____
Dr. Thomas Suleski

_____
Dr. James Conrad

ABSTRACT

CHARLOTTE SUSAN DULANEY STAHL. Vortices in coherent and partially coherent optical beams. (Under the direction of DR. GREGORY GBUR)

Vortices in optical beams have been the subject of extensive study since their status as a generic feature of light was established. They have found extensive use in optical trapping systems, astronomy, microscopy and are being investigated for free space communication systems. Related to optical vortices are correlation vortices in the coherence functions of partially coherent beams. Partially coherent beams have attracted interest as information carriers because of their resistance to scrambling on propagation. However, their analysis is more difficult than that of fully coherent beams due to the necessity of using correlation functions which increases the dimensionality of the integrals needed.

In this dissertation we demonstrate a complete description of a partially coherent vortex beam on propagation, and derive a new partially coherent beam class based on Laguerre-Gauss beams. We also give an analytic description of diffraction through any polygonal aperture, and demonstrate the triangular aperture case. We conclude with a study of fully coherent, partially coherent and incoherent beams propagated through turbulence.

ACKNOWLEDGEMENTS

I would like to thank Dr. Greg Gbur for all his shared knowledge, guidance, mentoring and patience over the course of this work.

Thanks are also due to the Department of Optical Science and Engineering and the Graduate School for GASP scholarships, and the Air Force Office of Scientific Research (AFOSR) for their support through grant (FA9550-16-1-0240).

DEDICATION

To my family, who set me on this path and saw me through to the end.

TABLE OF CONTENTS

LIST OF FIGURES

LIST OF TABLES

LIST OF ABBREVIATIONS

BWVB Beam wander vortex beam

CAB Coherent array beam

DFT Discrete Fourier Transform

FFT Fast Fourier Transform

GSM Gaussian Schell model

ICAB Incoherent array beam

LG Laguerre-Gauss

LGVB Laguerre-Gauss vortex eam

OAM Orbital angular momentum

PCVB Partially coherent vortex beam

SVCB Single vortex coherent beam

CHAPTER 1: HISTORY

Research into partially coherent vortex beams is the convergence of two different branches of optical research, one dealing with topological phase properties of propagating fields and one dealing with the statistical properties of light. The first branch is *singular optics*, which is a relatively young field that examines vortices (or singularities) which occur as a typical feature in coherent wave fields. The second is *optical coherence theory*, elements of which began to appear in the 19th century but took off in earnest in the 1930s. Optical coherence theory examines the effects of random fluctuations on observed properties of light. At their intersection is research into correlation singularities in partially coherent beams.

1.1 Optical coherence theory

Coherent light has been a critical component of optics for over two centuries. Fully coherent light is completely correlated in both spatial and temporal dimensions. The monochromatic plane wave of thought-experiments and simplified optical calculations is in essence a wave that has complete spatial and temporal coherence. Each wavefront is perfectly uniform and the phase undergoes no variation at all. In practice, light must be specially prepared to have the necessary criteria to approximate this mathematical nicety. Take for example Young's two pinhole experiment, which demonstrated the wave-like nature of light. It relies on spatially coherent light in order to produce the well-known fringe pattern. In order to conduct this experiment in an age well before lasers, which now cheaply provide the coherent, collimated beam required, Young used a mirror to direct sunlight onto a pinhole in a piece of thick card paper attached to a shutter so that the resulting beam of light projected onto the far

wall. In order to obtain the very narrow separation required between the split beam paths, he initially used a thin card, a knife's edge, a hair or fine wire [2]. Because sunlight is broadband, Young's interference patterns were colorful (see Figure 1.1) and allowed him to calculate the difference in "undulations" between red and purple light [2].

The celebrated Michelson-Morley experiment had even greater challenges in an age before lasers. Designed to detect drift in the "aether" or the medium which was imagined to support electromagnetic waves in a vacuum, their experiment was comprised of a two arm interferometer. The thought was that the earth, which moves very rapidly through space, would create "wind" in the aether and that this "wind" could be detected by the difference in speed between light traveling with it and orthogonal to it. An interferometer is limited by the coherence length of the light used, and the experimenters conducted the experiment with white light from an oil lamp rather than quasi-monochromatic light from a sodium lamp, despite its very short coherence length. Using an oil lamp as their light source, they had to precisely match the path lengths between the two arms of their interferometer, an engineering challenge in and of itself (see Michelson's diagram, Fig.1.4). The apparatus then had to be set up in a deep basement of a stone building, resting on top of a block of sandstone, floating on a pool of mercury [1] to eliminate vibration [1] . The results of this dedication to precision are the "most famous null result" that disproved the existence of aether as the medium through which light traveled.

Despite relying on high coherence for experiments, and having experience with the limitations of real light sources, there was only scattered interest in describing non-ideal or partially coherent light throughout the nineteenth and early twentieth centuries. In their classic text, "Principles of Optics", Born and Wolf cite Émile

[1] That this experiment worked at all is rather incredible. Michelson interferometers are so commonplace in physics labs and relatively easy to set up with cheap diode lasers that it's easy to gloss over the difficulty of this experiment until you see a picture of their original device and learn that Michelson had a nervous breakdown trying to get the data [3][Chapter 2]

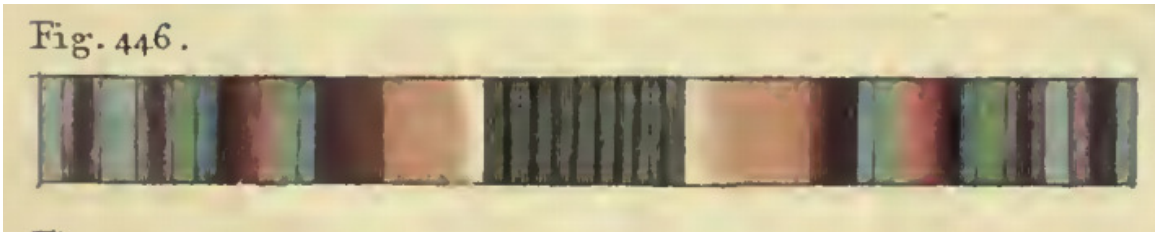

Figure 1.1: Young's illustration of sunlight diffracted around a wire, taken from the 1807 published edition of his lectures.

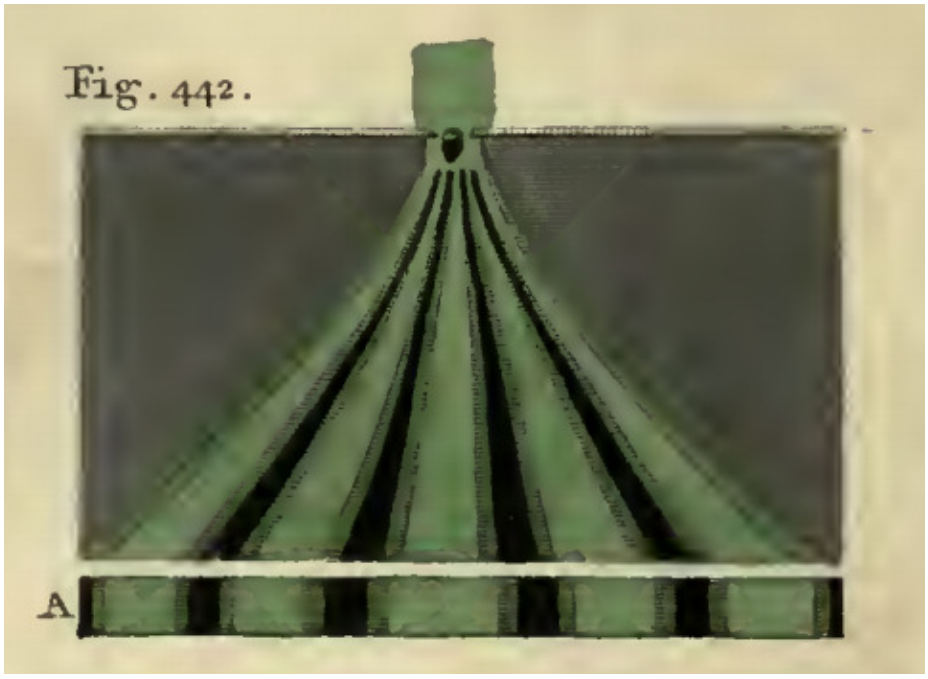

Figure 1.2: Young's schematic illustration of two pinhole diffraction, taken from the 1807 published edition of his lectures.

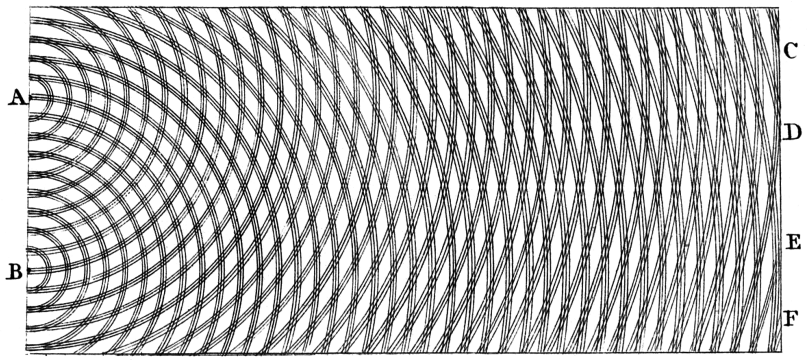

Figure 1.3: Young's original drawing showing his conceptualization of the wave fronts emerging from the pinholes and interfering, based on his observation of water waves.

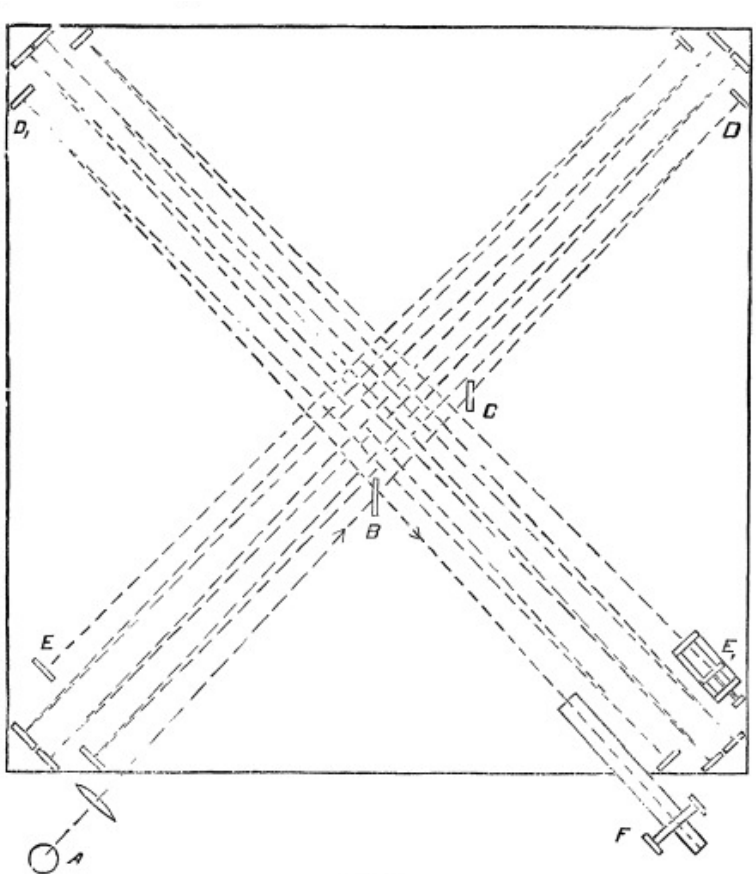

Figure 1.4: A schematic diagram of the Michelson-Morley interferometer. Light from an oil lamp at A is collected and sent to a half-silvered mirror at B, where the light is split. Each beam takes multiple trips between mirrors before being sent to the telescope at F. The difference in path length can be controlled by a screwed mirror at E_1, and a compensator plate at C makes up the path difference from passing through rather than being reflected by the half-silvered mirror. [1]

Verdet's 1865 paper "Étude sur la constitution de la lumiere non polarisée et de la lumiere partiellement polarisée" [4] as the first paper to investigate the subject of partial coherence as part of a theoretical calculation of the coherence of sunlight. There followed some fitful interest in partial coherence in relation to other problems. Michelson investigated the relationship between fringe visibility in the 1890s [5, 6, 7] and the intensity distribution at the source, but this work was not linked to coherence effects until later [8]. There was another lull in developments until 1907 when von Laue published the first quantitative measurements of the correlation of "light vibrations" [8] in connection with his study of the thermodynamics of light [9]. Berek made additional contributions, as it related to his work on image formation in microscopes [10, 11].

Partial coherence begins to finally be studied in its own right with van Cittert in 1934 [12], who derived the joint probability distribution for the product of fields at any two points on a screen when illuminated by a planar source of finite extent, and in 1939 derived the probability distribution for the product of fields at a single point at two different times illuminated by a source of finite extent [13]. A simpler method was determined by Zernike, who defined the "degree of coherence" of lightwaves in relation to quantities susceptible to experimental verification. While Zernike's degree of coherence is essentially the same as van Cittert's correlation coefficients, it had the advantage of being easier to apply to practical problems [8, Section 10.1]. Their two approaches were later combined into the van Cittert-Zernike theorem, which has proven to be particularly useful for problems in astronomy. However, while this work did begin to fill in the gap between coherent light and incoherent light, it was only narrowly applicable to spatially incoherent sources and small path differences. For the field to truly blossom, a more general approach was required. This was accomplished independently by Wolf [14], and Blanc-Lapierre and Dumontet [15], though Wolf is now the best known of the formulators. They introduced more general correlation

functions to the study of partial coherence, and discovered that the correlation functions obey a pair of wave equations (now known as the Wolf equations), implying that the correlations in wave fields propagate along with the actual electromagnetic disturbances. Additional coherence functions have been added as the field has developed, allowing for the study of increasingly complicated scenarios. The twenty-first century has ushered in the understanding that coherence and polarization are not entirely separable effects but two facets of how lightwaves may be organized [16][Preface].

1.2 Singular Optics

In wave mechanics, a singular point occurs wherever the amplitude (or, equivalently, intensity) of the wavefield drops to zero, and the phase becomes, by mathematical necessity, undefined. If the singular point occurs in a fluid, such as the ocean, it may manifest as a point which neither rises nor falls with the tide [17], with such points being known as amphidromies. In optics, such points appear as dark regions if the field is projected onto a screen, such as occurs in Young's two pinhole experiment (see Figure 1.2). These areas have become known as *phase singularities*. Such areas of null intensity caused by the wave nature of light have been known about as long as the wave theory of light, but have historically attracted little attention. What was of interest in Young's two pinhole experiment was not the bands of darkness, but the bands of light. Even 161 years after light's wave-like nature was proven by the aforementioned experiment, so-called singular areas attracted little interest as exemplified by this quotation from Arnold Sommerfeld's 1964 monograph *Optics* [18]:

> Visual inspection shows that there are finite regions, several wavelengths in extent, which have, to a sufficient degree of approximation, the character of a homogeneous plane wave and also retain this character as the wave propagates. Hence, these regions indeed satisfy the above postulated condition for regions of good approximation. Only the zero points seem to be exceptions. However, just because the amplitude van-

> ishes there, they do not produce any stronger effect than other points of varying intensity.

It would take another ten years before Nye and Berry would argue that the accepted wisdom was misguided with their seminal 1974 paper "Dislocations in wavetrains" [19] which demonstrated that the phase structure around singular points is very similar to the defects found in crystals, known as dislocations. They were able to show that this was no mere mathematical curiosity but rather that these were the generic, or "typical", features in propagating wavefields. Any system where three or more wavefronts interfere will exhibit dislocations. In this sense, Young's two pinhole diffraction pattern is not generic.

Crystal dislocations are defects in regular crystalline structures and may have one of several forms: edge, screw, or mixed edge-screw. An edge dislocation occurs when one plane is forced in between two others, as seen in Fig 1.5(a). A screw dislocation occurs when one portion of the crystal is forced to slip, but reconnects to form a helical lattice, as seen in Fig 1.5(b), much like a spiral staircase. A mixed edge screw shows features of both. Nye and Berry were able to demonstrate theoretically all three types of dislocations occurred around optical phase singularities, but found screw and mixed to be more typical. These structures have come to be known as *optical vortices*, since the most common dislocation, the screw type, is reminiscent of the vortices seen in fluids.

In their paper, Nye and Berry examine how the phase structure of beams with singularities resembles the different types of crystal dislocations. This undercut the assumption that just because there was little intensity there was little of interest in the area of null points. On the contrary, a whole host of interesting and, as would later be discovered, useful phenomena occur around points of zero intensity. While producing stable, coherent vortex modes may present challenges that will be discussed in a later section, optical vortices are ubiquitous. As Nye put it, "These are threads

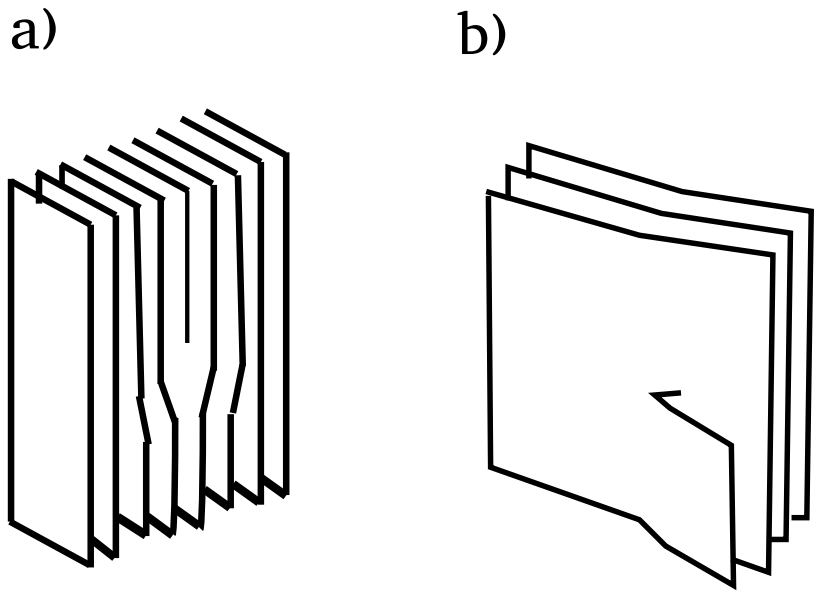

Figure 1.5: Schematic diagram of a) edge dislocations and b) screw dislocations.

of nothingness that exist, in general, in all wave fields, and they turn out to be phase singularities." [20]

The field of singular optics developed as researchers set about learning about these previously ignored vortices and describing their behavior[2]. A major development was the discovery that light can carry not just spin angular momentum as predicted by Poynting [22] and measured by Beth [23], but also orbital angular momentum (OAM). This OAM is closely associated with the presence of optical vortices.

Singular optics has over the past few decades also yielded practical results. Optical spanners and tweezers make the manipulation of small objects without mechanical contact possible [24], such as capturing or rotating cells, which is of particular use to biologists, while arranging multiple vortices can create microfluidic pumps [25]. Optical vortex coronagraphy expands the information gathering powers of telescopes [26]; optical vortices can also be used in phase contrast microscopy [27]. They also show promise for use in free space optical communication [28], as vortex beams are more stable under perturbation than non-vortex beams, thanks in part to their orbital

[2]A curious parallel to a more familiar, and imagination capturing, vortex structure has been explored separately by both Nye [21] and Berry [17], that of the tidal whirlpool.

angular momentum.

1.3 Coherence Vortices

On the face of it, it may have seemed unlikely that coherence theory would overlap with singular optics. Partially coherent fields do not have zeros of intensity as a generic feature, and their phase is not well-defined. Since phase singularities require both a well-defined phase and spots of zero intensity, it would be reasonable not to expect optical vortices in such beams.

This expectation was challenged by Schouten *et alia* in 2003 [29], when they theoretically predicted correlation singularities in the special case of Young's two pinhole experiment conducted with partially coherent light. These correlation singularities, like the zeros in a Young's experiment with coherent light, are nongeneric. But this observation sparked a series of independent investigations by several research groups into these unusual structures. Gbur and Visser investigated correlation singularities in partially coherent beams [30], while Freund demonstrated their occurrence in optical Lissajous fields [31]. Bogatyryova *et alia* proposed and implemented a method for creating partially coherent beams with both optical and correlation vortices [32], and Palacios *et alia* demonstrated correlation singularities in the cross-correlation function of a partially coherent vortex beam [33]. Work continued with the characterization of a type of partially coherent Laguerre Gauss beam of the first order in the waist plane [34], and characterization of the orbital angular momentum carried by such partially coherent beams [35].

CHAPTER 2: OPTICAL PRELIMINARIES

In this chapter we lay out some of the foundations for the research contained in the following chapters.In particular we will provide a mathematical introduction to singular optics and coherence theory. We will largely concern ourselves with studies involving the class of beams known as Laguerre-Gauss (LG) beams, which are scalar wavefields with a vortex structure. In Chapter 3, we investigate the behavior of the cross spectral density function of an ensemble of LG beams, and we will introduce and define for the cross spectral density function in this chapter.

2.1 Singular Optics

To begin, we examine a strictly monochromatic scalar plane wave,

$$V(\mathbf{r},t) = U(\mathbf{r})\exp[-i\omega t], \tag{2.1}$$

where $U(\mathbf{r})$ is the space dependent component which, in vacuum, must satisfy the Helmholtz equation,

$$(\nabla^2 + k^2)U = 0, \tag{2.2}$$

where ∇^2 is the Laplacian operator and $k = \omega/c$. This is also known as the time-independent wave equation, and can be used to solve for a wave's propagation. To introduce a simple vortex structure, we may approximate $U(\mathbf{r})$ in the plane $z = 0$ as

$$U(\rho,\phi) = \rho\exp\left[\pm i\phi\right] = x \pm iy. \tag{2.3}$$

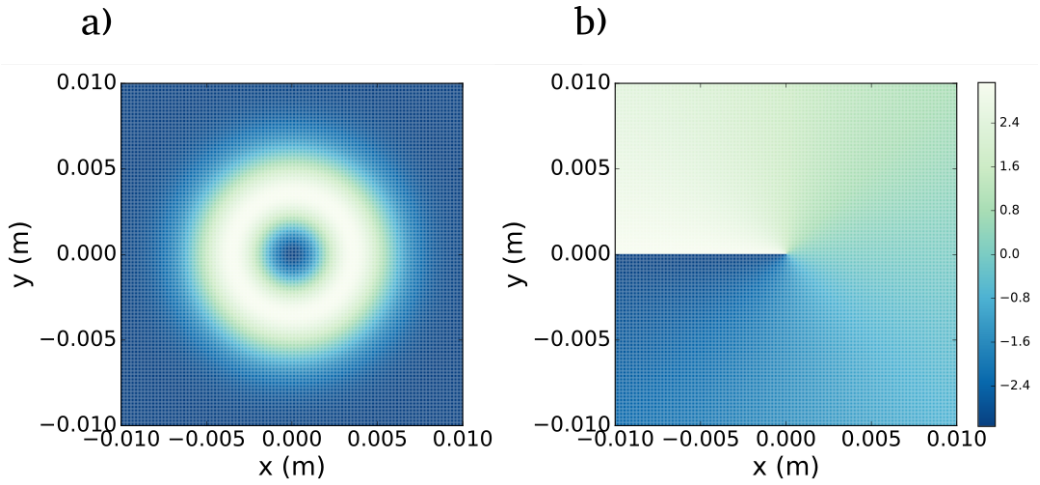

Figure 2.1: Plot of the simplest type of vortex beam, m=1. a) Intensity plot showing the null spot in the center and b) phase plot.

This describes, locally near the origin, a vortex whose core extends along the z-axis.

Because of the requirement that the field must be continuous, the amplitude must go to zero at the origin, and so the phase is undefined. For $\rho > 0$, ϕ increases in a right-handed or left handed spiral, depending on the sign in the exponent. It is only because the phase is undefined at the central point that it is able to take on, effectively, all values between 0 and 2π around that point. This is illustrated in Figure 2.1(b).

In describing optical vortex beams, this basic mathematical descriptor of a vortex is paired with a Gaussian envelope to limit the intensity as in an actual system the transverse intensity. So, in the waist plane, the lowest order vortex beams could be written

$$u(x, y) = (x \pm iy) \exp\left[\frac{(x^2 + y^2)}{w^2}\right], \tag{2.4}$$

where w defines the width of the Gaussian envelope. The intensity of such a beam can be seen in 2.1(a). We may also introduce higher-order vortex beams, for which the phase changes by $\pm 2\pi m$ in a closed counterclockwise path about the origin, in

the form

$$u(x,y) = (x \pm iy)^m \exp\left[\frac{(x^2+y^2)}{w^2}\right]. \tag{2.5}$$

More properties of vortices will be discussed in the following chapters.

2.2 Laguerre-Gauss Beams

The simplest class of pure vortex beams are the Laguerre-Gauss (LG) beams, which are solutions to the paraxial wave equation in cylindrical coordinates and are relatively easy to produce experimentally. They can be produced in single mode lasers with cylindrically symmetric cavities [36], by passing a Gaussian beam through a spiral phase plate [37], or through a computer generated hologram [38]. The have the format of Eq. (2.5) in the waist plane. As a complete orthonormal set of solutions to the paraxial wave equation, they may be written as

$$\begin{aligned} U_m^n(x,y,z) =& \sqrt{\frac{2n!}{\pi w_0^2 (n+|m|)!}} \left(\frac{\sqrt{2}(x \pm iy)}{w(z)}\right)^{|m|} L_n^{|m|}\left(\frac{2(x^2+y^2)}{w_z^2}\right) \\ & \times \exp\left[\frac{-(x^2+y^2)}{\sigma^2}\right] \exp\left[-i\Phi(z)\right] \end{aligned} \tag{2.6}$$

per [39, Chapter 2.2] where

$$\frac{1}{\sigma^2} = \frac{1}{w_z^2} + \frac{ik}{R_z}, \tag{2.7}$$

with the beam width on propagation being

$$w_z = w_0 \sqrt{1 + \left(\frac{z}{z_0}\right)^2}, \tag{2.8}$$

and the radius of curvature on propagation being

$$R_z = z\left[1 + \left(\frac{z_0}{z}\right)^2\right], \tag{2.9}$$

both of which depend on the Rayleigh range, which is defined as the distance at which the beam width is $\sqrt{2}w_0$,

$$z_0 = \frac{\pi w_0^2}{\lambda}, \tag{2.10}$$

where w_0 is the radius of the beam at its waist and λ is the wavelength. The wavenumber k is defined as

$$k = \frac{2\pi}{\lambda}, \tag{2.11}$$

and $\Phi(z)$ is the Gouy phase shift,

$$\Phi(z) = \arctan(z/z_0). \tag{2.12}$$

The intensity and phase for several beams of this type are shown in Figure 2.2.

We limit ourselves in the follow chapters primarily to discussions of beams that have a zero radial index ($n = 0$) and a non-zero azimuthal index ($m \neq 0$). These beams have a central singularity around which the phase increases, and lack ring dislocations in the radial direction. In such cases, the Laguerre polynomial term simplifies to

$$L_0^{|m|}\left[\frac{2(x^2+y^2)}{w^2(z)}\right] = 1. \tag{2.13}$$

Furthermore, the Gouy phase term, $\Phi(z)$, has no impact on the following calculations and simulations; in most cases it vanishes when the cross spectral density is first calculated. It represents a constant phase in any z-plane and so will not affect the location or types of singularities. Thus any leading coefficients to the equation as a whole have no impact on the phase structure of the correlation singularities. The normalization coefficients can be grouped together into a single, real term

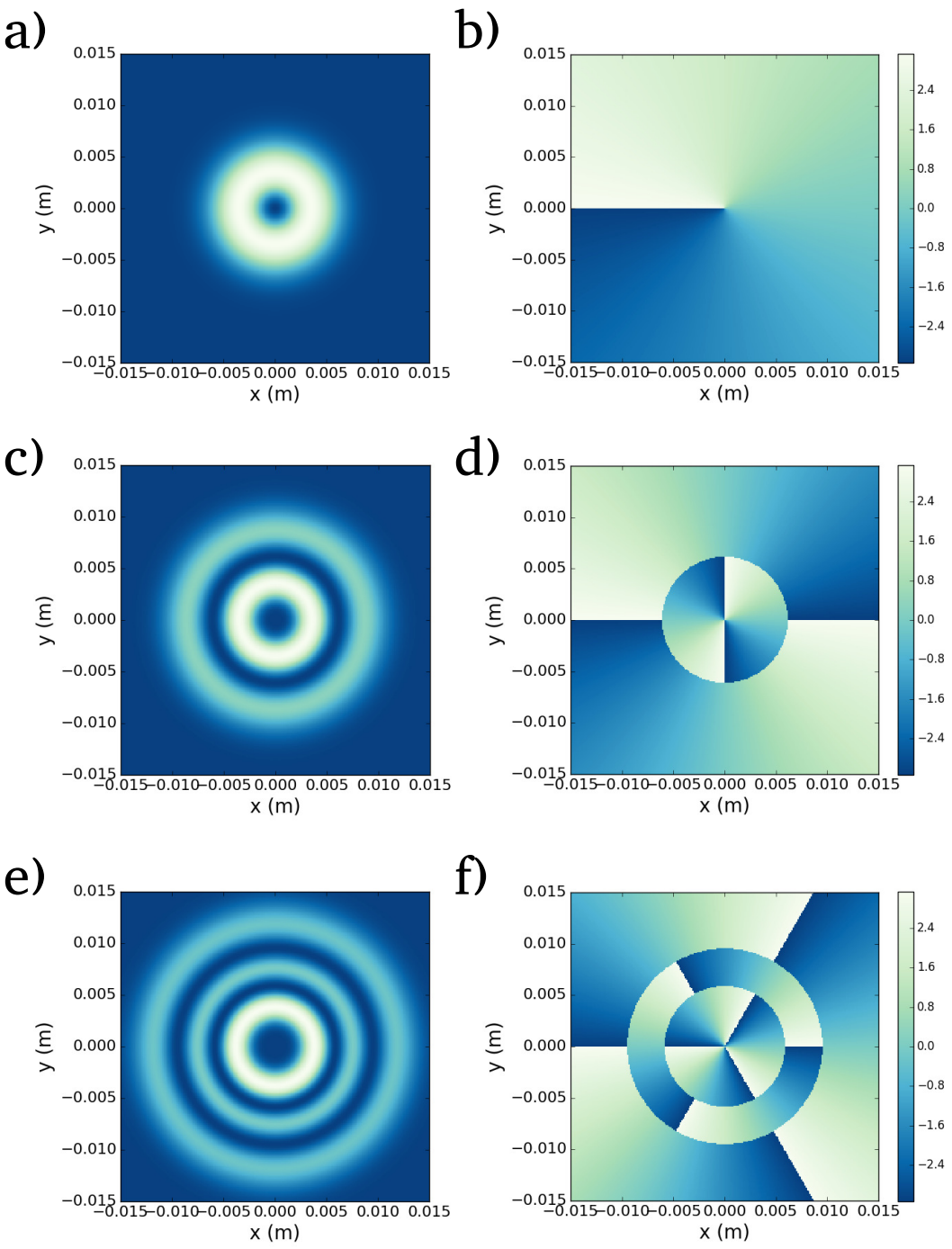

Figure 2.2: Examples of Laguerre Gauss beams in the waist plane, with $w_0 = 5$ mm. The a) intensity and b) phase plots for a beam with $m = 1$, $n = 0$. The c) intensity and d) phase plots for a beam with $m = 2$, $n = 1$. The c) intensity and d) phase plots for a beam with $m = -3$, $n = 2$.

$$C = \sqrt{\frac{2}{\pi w_0^2 (|m|)!}} \left(\frac{\sqrt{2}}{w_z}\right)^{|m|}. \tag{2.14}$$

Thus we are left with a much simplified formula for the beams of interest,

$$U_m(x, y, z) = C(x \pm iy)^{|m|} \exp\left[\frac{-(x^2 + y^2)}{\sigma^2}\right], \tag{2.15}$$

which will be used for the remainder of this dissertation. This form has the advantage of making the transverse structure of the beam easier to interpret. The single exponential term determines the transverse beam envelope and wavefront curvature while the $(x \pm iy)$ term controls the vortex structure.

2.3 Cross-Spectral Density Function

When dealing with partially coherent beams, the mutual coherence function has historically been the quantity of choice to describe coherence properties. The quantity

$$\Gamma(\mathbf{r}_1, \mathbf{r}_2, \tau) = \langle V^*(\mathbf{r}_1, t) V(\mathbf{r}_2, t + \tau) \rangle \tag{2.16}$$

is the space-time formulation of the cross-correlation function of time averaged fields [40, Section 4.3], where $V(\mathbf{r}, t)$ is the wavefield which is statistically stationary in the wide sense, and $\langle ... \rangle$ represents a time average. In 1955 Wolf described how this mutual coherence function satisfies a pair of wave equations,

$$\nabla_1^2 \Gamma(\mathbf{r}_1, \mathbf{r}_2, \tau) - \frac{1}{c^2} \frac{\delta^2}{\delta \tau^2} \Gamma(\mathbf{r}_1, \mathbf{r}_2, \tau) = 0, \tag{2.17}$$

$$\nabla_2^2 \Gamma(\mathbf{r}_1, \mathbf{r}_2, \tau) - \frac{1}{c^2} \frac{\delta^2}{\delta \tau^2} \Gamma(\mathbf{r}_1, \mathbf{r}_2, \tau) = 0, \tag{2.18}$$

implying that the mutual coherence function propagates in a similar manner to a coherent wave.

More recently it has been realized that the cross-spectral density, which is the Fourier temporal transform of the mutual coherence function, allows researchers to more easily find analytic solutions to second-order coherence phenomena. The cross-spectral density is defined as

$$W(\mathbf{r}_1, \mathbf{r}_2, \omega) = \frac{1}{2\pi} \int_{-\infty}^{\infty} \Gamma(\mathbf{r}_1, \mathbf{r}_2, \tau) \exp\left[i\omega\tau\right] d\tau. \tag{2.19}$$

It has been shown [41] that the cross spectral density function may be expressed as an average of an ensemble of monochromatic realizations of the field for any partially coherent field at frequency ω, written as

$$W(\mathbf{r}_1, \mathbf{r}_2, \omega) = \left\langle U^*(\mathbf{r}_1, \omega), U(\mathbf{r}_2, \omega) \right\rangle_\omega, \tag{2.20}$$

where $\langle ... \rangle_\omega$ indicates an average over the frequency ensemble, and allows for the determination of the cross spectral density of a wavefield without first having to find the mutual coherence function.

Like the mutual coherence function, cross spectral density function obeys a pair of wave equations in the absence of sources [16, Section 4.1], in this case the Helmholtz equations

$$[\nabla_j^2 + k^2] W(\mathbf{r}_1, \mathbf{r}_2, \omega) = 0, \;\; j = 1, 2, \tag{2.21}$$

which are comparable to the equations for a monochromatic field, Eq. (2.2). It follows that with one observation point fixed, it behaves in an identical manner to a monochromatic wavefield and is capable of demonstrating the same types of behavior, including vortices with the same phase and topological characteristics. These vortices are known as *correlation vortices*, sometimes also called coherence vortices in earlier works. Although it has been shown that they are closely related [42], correlation

vortices are distinct from optical vortices in several important ways. While optical vortices are phase singularities occurring around null-points in the wavefield, and thus their location is set, the location of correlation vortices is heavily dependent on the choice of observation point since the cross spectral density is a two-point correlation function. Thus while optical and correlation vortices are related, they are physically distinct features.

In principle, the formulation above is exact, and correlation singularities can exist for every frequency in a partially coherent field and at different locations for each of those frequencies. However, this dissertation will restrict itself to the case of a quasi-monochromatic wavefield, where $\Delta\omega \ll \omega_0$ and the field appears monochromatic over many cycles. We will drop ω from the cross-spectral density from here on for notational brevity.

A few additional quantities related to the cross-spectral density will be useful in the following sections. The spectral density function,

$$S(\mathbf{r}) = W(\mathbf{r}, \mathbf{r}), \tag{2.22}$$

which gives the intensity at a frequency ω, and for a quasi-monochromatic field is a good representation of the intensity. We will also use the spectral degree of coherence

$$\mu(\mathbf{r}_1, \mathbf{r}_2) = \frac{W(\mathbf{r}_1, \mathbf{r}_2)}{\sqrt{W(\mathbf{r}_1, \mathbf{r}_1)W(\mathbf{r}_2, \mathbf{r}_2)}}. \tag{2.23}$$

It can be shown that $0 < |\mu| < 1$, with 0 indicating incoherence and 1 being full coherence. From these definitions it follows that

$$W(\mathbf{r}_1, \mathbf{r}_2) = \sqrt{S(\mathbf{r}_1)S(\mathbf{r}_2)}\mu(\mathbf{r}_1.\mathbf{r}_2), \tag{2.24}$$

which we will take advantage of in the following section.

2.4 Gaussian Schell-Model Beams

One type of beam that is frequently encountered in optical coherence theory is the Gaussian Schell model (GSM) beam. Schell-model sources are defined as sources for which their spectral degree of coherence, $\mu(\boldsymbol{\rho}_1, \boldsymbol{\rho}_2, \omega)$, depends only on the difference in position between observation points $\boldsymbol{\rho}_1$ and $\boldsymbol{\rho}_2$, so that their spectral degree of coherence may be expressed as $\mu(\boldsymbol{\rho}_2 - \boldsymbol{\rho}_1, \omega)$ [16, Section 5.3.1]. Thus a Schell model source will have a cross spectral density

$$W(\boldsymbol{\rho}_1, \boldsymbol{\rho}_2, \omega) = \sqrt{S(\boldsymbol{\rho}_1)}\sqrt{S(\boldsymbol{\rho}_2)}\mu(\boldsymbol{\rho}_2 - \boldsymbol{\rho}_1, \omega). \tag{2.25}$$

where $S(\boldsymbol{\rho})$ is the spectral density function. If, additionally, the source is locally coherent, then it will be able to form a beam [43].

In the case of a Gaussian Schell model sources, we add the additional constraint that the spatial distribution of its spectral density and its spectral degree of coherence are Gaussian. This creates an analytically tractable model of a source with with a variable coherence, as can seen with a simple example. Consider a GSM beam with a spectral density

$$S(\boldsymbol{\rho}_1 + \boldsymbol{\rho}_2) = A^2 \exp[-\rho^2/2\sigma_s^2] \tag{2.26}$$

and a spectral degree of coherence

$$\mu(\boldsymbol{\rho}_2 - \boldsymbol{\rho}_1) = \exp[-(\boldsymbol{\rho}_2 - \boldsymbol{\rho}_1)^2/(2 * \sigma_\mu^2)]. \tag{2.27}$$

In the limit as $\sigma_\mu \to \infty$, the spectral degree of coherence approaches unity and the source is fully coherent. This is of course an idealize GSM source. If we consider instead a quasi-monochromatic circular source of radius a though this limit must be interpreted with some caution, since it assumed that $a >> \sigma_\mu$ and the source cannot

be infinite in size. However, this can usefully model real laser sources operating in the lowest Hermite-Gauss modes [16, Section 5.3.1].

CHAPTER 3: PARTIALLY COHERENT VORTEX BEAMS

This chapter deals with the derivation and properties of a new class of partially coherent vortex beams (PCVBs). We begin with a description of the beam wander model, which we use to derive the characteristics of partially coherent beams in an analytically tractable manner. The second section details the properties of the first order vortex case on propagation, previously published in [44], while the third section is concerned with the creation of an infinite class of PCVBs and their behavior at higher orders, previously published in [45].

3.1 Beam Wander Model

It is difficult to derive coherence properties directly from physics, so we must employ models. Such models, to be most useful, should allow us to make beams with any spatial coherence. This role is fulfilled by the beam wander model, where by the cross-spectral density is modified to be

$$W(\mathbf{r}_1, \mathbf{r}_2) = \int U_{\pm}^*(\mathbf{r}_1 - \mathbf{r}_0, z_1) U_{\pm}(\mathbf{r}_2 - \mathbf{r}_0, z_2) f(\mathbf{r}_0) d^2\mathbf{r}_0, \tag{3.1}$$

where

$$f(\mathbf{r}) = \frac{1}{\pi\delta} \exp\left[\frac{-\mathbf{r}^2}{\delta^2}\right], \tag{3.2}$$

which introduces fluctuations into the field by allowing the position of the core of the beam to be a random vector with a Gaussian distribution, the width of which can be increased or decreased to model a particular degree of coherence. That is, the beam "wanders" around the origin. If it wanders only slightly ($\delta \approx 0$) then the beam

approximates the fully coherent case. The more it is allowed to wander, the lower the spatial coherence [1]. An increase in δ corresponds to a decrease in coherence, while a small δ corresponds to a more coherent beam. As a rule of thumb, the beam begins to exhibit behavior noticeably different from the coherent case when δ is the same order of magnitude as the beam width. This model was first used by Gbur *et alia* to investigate the existence of correlation singularities in quasi-monochromatic, partially coherent wavefields [46]. It should be noted that PCVBs are not purely theoretical constructs. Partially coherent vortex beams have been generated experimentally using a variety of techniques, including coherent sources and computer generated holograms [47] and incoherent sources and spiral phase plates [48].

3.2 Complete Representation of a 1st order LG beam on propagation

Before addressing the derivation of an entire class of vortex beams, it is helpful to fully understand the lowest order case. While several papers address the characteristics of the partially coherent first-order Laguerre-Gauss beam in the waist plane (e.g., [46, 49]) the behavior of such a beam on propagation has not yet been elucidated. This was in part due to the difficulty in addressing the additional dimensions needed because of the doubling of variables in a correlation function. A field in a transverse plane requires two variables, while its corresponding correlation function requires four. Likewise, to describe a field on propagation requires three variables, and its correlation function requires six.

3.2.1 Derivation

We begin with the beam wander model as described in the previous section (3.1), and the simplified LG beam (2.15) with $m = \pm 1$,

[1] To speak extremely casually, but visually, it may be thought of as a laser mounted on a washing machine. If the washer is off, it does not wander at all, and the beam remains coherent. If the washer is doing a normal load, there is some vibration, and some blurring of the beam, but some coherent effects remain. If the washer is spinning an unbalanced load of towels, the beam is shaking all over the place and is effectively incoherent.

$$W(x_1,y_1,z_1;x_2,y_2,z_2) = \frac{|C|^2}{\pi\delta}\int\Big[(x_1-x_0)\mp(y_1-y_0)\Big] \times\exp\left\{-\frac{1}{\tilde{\sigma}_1^2}\left((x_1-x_0)^2+(y_1-y_0)^2\right)\right\} \times\Big[(x_2-x_0)\pm(y_2-y_0)\Big] \times\exp\left\{-\frac{1}{\sigma_2^2}\left((x_2-x_0)^2+(y_2-y_0)^2\right)\right\} \times\exp\left\{\frac{-(x_0^2+y_0^2)}{\delta^2}\right\}dx_0dy_0, \tag{3.3}$$

where $\tilde{\sigma_n^2}$ is the complex conjugate of σ_n^2 for $n=1,2$. This integral can be evaluated analytically with some effort. We begin by grouping exponents and completing the square such that

$$A \equiv \frac{1}{\tilde{\sigma}_1^2}+\frac{1}{\sigma_2^2}+\frac{1}{\delta^2}, \tag{3.4}$$

$$B_x = \frac{x_1}{\tilde{\sigma}_1^2}+\frac{x_2}{\sigma_2^2}, \tag{3.5}$$

$$B_y = \frac{y_1}{\tilde{\sigma}_1^2}+\frac{y_2}{\sigma_2^2}, \tag{3.6}$$

so the integral becomes

$$W(\mathbf{r}_1,\mathbf{r}_2) = D(\mathbf{r}_1,\mathbf{r}_2)\int\Big[(x_1-x_0)\mp i(y_1-y_0)\Big]\Big[(x_2-x_0)\pm i(y_2-y_0)\Big] \times\exp\left\{-A(x_0-B_y/A)^2\right\}\exp\left\{-A(y_0-B_y/A)^2\right\}dx_0dy_0, \tag{3.7}$$

$$\mathbf{r}_n = (x_n,y_n,z_n), \quad n=1,2,$$

where

$$D(\mathbf{r}_1,\mathbf{r}_2)=\frac{|C|^2}{\pi\delta}\exp\left\{\frac{B_x^2}{A}+\frac{B_y^2}{A}-\frac{1}{\tilde{\sigma}_1^2}(x_1^2+y_1^2)-\frac{1}{\sigma_2^2}(x_2^2+y_2^2)\right\}. \tag{3.8}$$

By expanding the terms in the square brackets, we can rewrite the single integral as four separate integrals

$$\begin{aligned}W(\mathbf{r}_1,\mathbf{r}_2)&=D(\mathbf{r}_1,\mathbf{r}_2)\\
&\times\Bigg[(x_1\mp iy_1)(x_2\pm iy_2)\int\exp\left\{-A(x_0-B_x/A)^2\right\}\exp\left\{-A(y_0-B_y/A)^2\right\}dx_0dy_0\\
&-(x_2\pm iy_2)\int(x_0\mp iy_0)\exp\left\{-A(x_0-B_x/A)^2\right\}\exp\left\{-A(y_0-B_y/A)^2\right\}dx_0dy_0\\
&-(x_2\mp iy_1)\int(x_0\pm iy_0)\exp\left\{-A(x_0-B_x/A)^2\right\}\exp\left\{-A(y_0-B_y/A)^2\right\}dx_0dy_0\\
&+\int(x_0^2+y_0^2)\exp\left\{-A(x_0-B_x/A)^2\right\}\exp\left\{-A(y_0-B_y/A)^2\right\}dx_0dy_0\Bigg],\end{aligned} \tag{3.9}$$

of known solutions. Thus we may write the cross-spectral density as

$$\begin{aligned}W(\mathbf{r}_1,\mathbf{r}_2)&=D(\mathbf{r}_1,\mathbf{r}_2)\frac{\pi}{A^2}\exp\{B_x^2+B_y^2\}\\
&\times\big[(x_1\mp iy_1)(x_2\pm iy_2)+B_x(-x_1-x_2-iy_2+iy_1)\\
&+B_y(-ix_1+ix_2+y_1+y_2)+B_x^2/A^2+B_y^2/A^2+1/A\big].\end{aligned} \tag{3.10}$$

This expression can be written more compactly by employing this somewhat lengthy list of definitions:

$$\frac{1}{\sigma_n^2} = \frac{1}{w_n^2} - \frac{ik}{2R_n}, \qquad n = 1, 2, \tag{3.11}$$

$$\frac{1}{\alpha_n^2} = \frac{1}{\delta^2} + \frac{1}{\sigma_n^2}, \qquad n = 1, 2, \tag{3.12}$$

$$\frac{1}{\beta_2^2} = \frac{1}{\delta^2} + \frac{1}{\sigma_1^{2*}} + \frac{1}{\sigma_2^2}, \tag{3.13}$$

$$w_n \equiv w(z_n), \qquad n = 1, 2, \tag{3.14}$$

$$R_n \equiv R(z_n), \qquad n = 1, 2, \tag{3.15}$$

$$Q = D\frac{\pi}{A^2}\exp\{B_x^2 + B_y^2\}, \tag{3.16}$$

with σ_n^2 describing the width of the Gaussian envelope of the beam and δ the degree of incoherence as previously mentioned. As described in Section 2.2, σ_n^2 depends on z_n through its dependence on the beam width (Eq. (2.8)) and Rayleigh range (Eq.(2.9)). Finally, Q is a complex, position dependent factor that nevertheless plays no role in the location of the zeros. Because we are only interested in those solutions where $\mathrm{Re}\{W\}$ and $\mathrm{Im}\{W\}$ are simultaneously zero, and Q is a common coefficient, it is divided out and has no effect on the location or structure of the correlation vortices. As such, it will be suppressed after its appearance in the equation below for the sake of brevity and clarity.

Thus armed with these definitions, we may with much effort write our solution in the pleasingly compact form

$$\begin{aligned} W(\boldsymbol{\rho}_1, \boldsymbol{\rho}_2, z_1, z_2) = Q\Bigg\{ &\left[\frac{1}{\alpha_2^2}(x_1 \mp iy_1) - \frac{1}{\sigma_2^2}(x_2 \mp iy_2)\right] \\ &\times \left[\frac{1}{\tilde{\alpha}_1^2}(x_2 \pm iy_2) - \frac{1}{\tilde{\sigma}_1^2}(x_1 \pm iy_1)\right] + \frac{1}{\beta_2^2}\Bigg\}. \end{aligned} \tag{3.17}$$

In order to locate the singularities in the cross-spectral density, we search for posi-

tions where the real and imaginary parts are simultaneously zero. As written above, Equation (3.17) is in six spatial variables. It can be shown that the cross-spectral density only equals zero when

$$z_1 = z_2 \equiv z. \tag{3.18}$$

This is more easily done using the results in the form of Eq.(3.10). We begin with the observation that everything outside the square brackets divides out when the equation is set to zero, and suppress them for the next stage of the calculation. Furthermore, A, B_x, and B_y are all complex, arising from their dependence on σ_1, σ_2. Thus they may be written as

$$A = \left(\frac{1}{w_{z_1}^2} + \frac{1}{w_{z_2}^2} + \frac{1}{\delta^2}\right) + i\left(\frac{k}{2R_{z_2}} - \frac{k}{2R_{z_1}}\right), \tag{3.19}$$

$$B_x = \left(\frac{x_1}{w_{z_1}^2} + \frac{x_2}{w_{z_2}^2}\right) + i\left(\frac{kx_2}{2R_{z_2}} - \frac{kx_1}{2R_{z_1}}\right), \tag{3.20}$$

$$B_y = \left(\frac{y_1}{w_{z_1}^2} + \frac{y_2}{w_{z_2}^2}\right) + i\left(\frac{ky_2}{2R_{z_2}} - \frac{ky_1}{2R_{z_1}}\right), \tag{3.21}$$

and with some effort the cross spectral density may be separated into its real and imaginary parts. We begin by looking at the imaginary part, which may be written

as

$$
\begin{aligned}
0 = {} & \pm x_1 y_2 \mp x_2 y_1 \\
& + \frac{1}{|A|^2}\Bigg\{(-x_1 - x_2)\left[\xi_x \mathfrak{b} - \left(\frac{x_1}{w_{z_1}^2} + \frac{x_2}{w_{z_2}^2}\right)\Upsilon\right] + (-y_1 - y_2)\left[\left(\frac{x_1}{w_{z_1}^2} + \frac{x_2}{w_{z_2}^2}\right)\mathfrak{b} + \xi_x \Upsilon\right] \\
& \qquad + (-x_1 + x_2)\left[\left(\frac{y_1}{w_{z_1}^2} + \frac{y_2}{w_{z_2}^2}\right)\mathfrak{b} + \xi_y \Upsilon\right] + (y_1 + y_2)\left[\xi_y \mathfrak{b} - \left(\frac{y_1}{w_{z_1}^2} + \frac{y_2}{w_{z_2}^2}\right)\Upsilon\right]\Bigg\} \\
& + \frac{1}{|A|^4}\Bigg\{2\xi_x\left(\frac{x_1}{w_{z_1}^2} + \frac{x_2}{w_{z_2}^2}\right)\left(\mathfrak{b}^2 - \Upsilon^2\right) + 2\mathfrak{b}\Upsilon\left[\left(\frac{x_1}{w_{z_1}^2} + \frac{x_2}{w_{z_2}^2}\right)^2 - \xi_x^2\right] \\
& \qquad + 2\xi_y\left(\frac{y_1}{w_{z_1}^2} + \frac{y_2}{w_{z_2}^2}\right)\left(\mathfrak{b}^2 - \Upsilon^2\right) + 2\mathfrak{b}\Upsilon\left[\left(\frac{y_1}{w_{z_1}^2} + \frac{y_2}{w_{z_2}^2}\right)^2 - \xi_y^2\right]\Bigg\} \\
& + \frac{\Upsilon}{\mathfrak{b}^2 - \Upsilon^2},
\end{aligned}
\tag{3.22}
$$

where

$$\mathfrak{b} = \frac{1}{w_{z_1}^2} + \frac{1}{w_{z_2}^2} + \frac{1}{\delta^2} \tag{3.23}$$

$$\Upsilon = \frac{k}{2R_{z_2}} - \frac{k}{2R_{z_1}} \tag{3.24}$$

$$\xi_x = \frac{kx_2}{2R_{z_2}} - \frac{kx_1}{2R_{z_1}} \tag{3.25}$$

$$\xi_y = \frac{ky_2}{2R_{z_2}} - \frac{ky_1}{2R_{z_1}} \tag{3.26}$$

$$\tag{3.27}$$

all of which depend on z_1, z_2 through the Rayleigh range and beam width. This monstrous expression becomes solvable, and indeed tractable, if

$$z_1 = z_2 = z. \tag{3.28}$$

In this case, A becomes entirely real

$$A = \frac{2}{w_z^2} + \frac{1}{\delta^2}, \tag{3.29}$$

and the term

$$\Upsilon = 0. \tag{3.30}$$

In this case, the expression simplifies greatly to

$$\begin{aligned}
0 = & \pm x_1 y_2 \mp x_2 y_1 \\
& + \frac{1}{A}(-x_1 - x_2)\left[\left(\frac{k(x_2 - x_1)}{2R_z}\right)\right] + \frac{1}{A}(-y_1 - y_2)\left[\left(\frac{x_1 + x_2}{w_z^2}\right)\right] \\
& + \frac{1}{A}(-x_1 + x_2)\left[\left(\frac{y_1 + y_2}{w_z^2}\right)\right] + \frac{1}{A}(y_1 + y_2)\left[\left(\frac{k(y_2 - y_1)}{2R_z}\right)\right] \\
& + \frac{1}{A^2}\left[2\left(\frac{x_1 + x_2}{w_z^2}\right)\left(\frac{k(x_2 - x_1)}{2R_z}\right)\right] \\
& + \frac{1}{A^2}\left[2\left(\frac{y_1 + y_2}{w_z^2}\right)\left(\frac{k(y_2 - y_1)}{2R_z}\right)\right].
\end{aligned} \tag{3.31}$$

As a check, we can evaluate this expression at the waist plane where $R_z = 0$, and find that it goes to zero when

$$\frac{x_1}{x_2} = \frac{y_1}{y_2} \tag{3.32}$$

which matches the conditions found by [34]. We can now return to Eq. (3.17) and proceed with the further simplified form

$$\begin{aligned}
W(\boldsymbol{\rho}_1, \boldsymbol{\rho}_2, z_1, z_2) = & \left\{ \left[\frac{1}{\alpha^2}(x_1 \mp i y_1) - \frac{1}{\sigma^2}(x_2 \mp i y_2)\right] \right. \\
& \left. \times \left[\frac{1}{\alpha^{2*}}(x_2 \pm i y_2) - \frac{1}{\sigma^{2*}}(x_1 \pm i y_1)\right] + \frac{1}{\beta_2^2}\right\}.
\end{aligned} \tag{3.33}$$

With this, we now investigate how zeros of W evolve.

3.2.2 Discussion

As noted, singularities of the cross-spectral density will occur where the real and imaginary parts are simultaneously equal to zero. The topology of these zeros (as will be seen in Section 3.3) is quite complex, especially when examined in terms of $\boldsymbol{\rho}_1$ and $\boldsymbol{\rho}_2$. It is therefore helpful, even necessary, to move onto a different coordinate system to study their behavior on propagation. Thus we introduce here the sum and difference coordinates

$$\begin{aligned} \boldsymbol{\rho}_+ &\equiv \frac{\boldsymbol{\rho}_1 + \boldsymbol{\rho}_2}{2}, \\ \boldsymbol{\rho}_- &\equiv \boldsymbol{\rho}_2 - \boldsymbol{\rho}_1, \end{aligned} \tag{3.34}$$

and the coefficients

$$\eta = \frac{1}{\alpha^2 \sigma^{*2}}, \tag{3.35}$$

$$2\chi = \left(\frac{1}{|\alpha|^4} + \frac{1}{|\sigma|^4} \right), \tag{3.36}$$

$$2Z = \left(\frac{1}{|\alpha|^4} - \frac{1}{|\sigma|^4} \right). \tag{3.37}$$

Using this simplified schema, the real and imaginary portions of the cross spectral density may be expressed as

$$\begin{aligned} \mathrm{Re}(W) = &-2\,\mathrm{Re}(\eta) \left[x_+^2 + y_+^2 + \frac{x_-^2 + y_-^2}{4} \right] \\ &+ 2\chi \left[x_+^2 + y_+^2 - \frac{x_-^2 + y_-^2}{4} \right] + \frac{1}{\beta_2^2}, \end{aligned} \tag{3.38}$$

$$\begin{aligned} \mathrm{Im}(W) = &\; 2i\,\mathrm{Im}(\eta) \left[x_+ x_- + y_+ y_- \right] \\ &\pm i2Z \left[x_+ y_- + y_+ x_- \right]. \end{aligned} \tag{3.39}$$

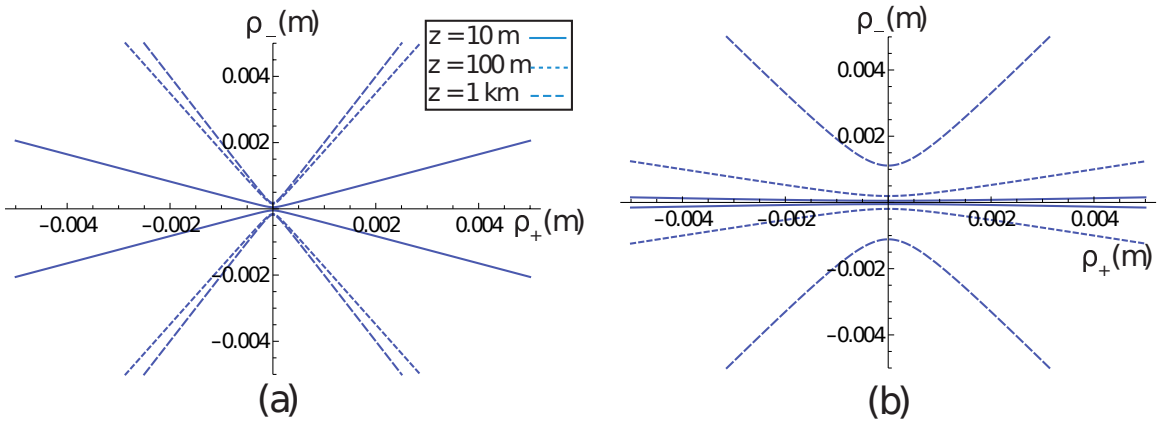

Figure 3.1: Zero manifolds of partially coherent beams on propagation in sum and difference coordinates. Radial positions a) slightly incoherent beam, ($\delta = 2$ mm) and b) moderately incoherent beam ($\delta = 8$ mm). In both figures, $w_0 = 1$ mm, $\lambda = 500$ nm

These equations may be further simplified by moving into polar coordinates and judicious use of trigonometric identities. By doing this we are able to see that the imaginary portion of the cross-spectral density is only zero when

$$\tan\Phi = \pm\frac{\mathrm{Im}(\eta)}{Z} \tag{3.40}$$

where $\Phi = \phi_+ - \phi_-$, which gives us an imaginary part that depends only on the angle between $\boldsymbol{\rho}_+$ and $\boldsymbol{\rho}_-$. Doing likewise to the real part yields

$$[-2\,\mathrm{Re}(\eta) + 2\chi]\rho_+^2 + \frac{1}{2}[-\mathrm{Re}(\eta) - \chi]\rho_-^2 + \frac{1}{\beta_2^2} = 0, \tag{3.41}$$

which depends solely on ρ_+, ρ_-, without any angular dependence.

The results of Equations (3.40) and (3.41) are plotted in Figure 3.1. Although the sum/difference coordinates may seem like they further remove the usefulness of our results, they permit several conclusions. Equation (3.41), for example, is a hyperbola for all distances, but the positioning of the hyperbolas is particularly interesting. While the arms of the hyperbolas for partially coherent beams lies between the ρ_+ and ρ_- axis, the more coherent the beam the more the hyperbola arms asymptotically

approach $\rho_- = 2\rho_+$. This is readily shown from Eq. (3.41). If we use the standard form for hyperbolas [50, Section 9.4]

$$\frac{x^2}{a^2} - \frac{y^2}{b^2} = 1, \tag{3.42}$$

we can easily find that for Eq. (3.41)

$$\frac{1}{a^2} = 2\beta_2^2(\mathrm{Re}\{\eta\} - \chi) \tag{3.43}$$

$$\frac{1}{b^2} = \frac{1}{2}\beta_2^2(-\mathrm{Re}\{\eta\} - \chi). \tag{3.44}$$

Using the formula for the asymptotes of hyperbolas [50, Section 9.4],

$$y = \pm\frac{b}{a}x \tag{3.45}$$

we see that

$$\boldsymbol{\rho}_- = 2\sqrt{\frac{\mathrm{Re}\{\eta\} - \chi}{-\mathrm{Re}\{\eta\} - \chi}}\boldsymbol{\rho}_+, \tag{3.46}$$

which if we take the limit as $\delta -> 0$, becomes

$$\boldsymbol{\rho}_- = 2\boldsymbol{\rho}_+. \tag{3.47}$$

This can be seen from Eq. (3.34) to be identical to the condition for fully coherent vortices that either $\rho_1 = 0$ or $\rho_2 = 0$. Figure 3.1(a) shows the hyperbolas for a slightly incoherent beam, and Figure 3.1(b) that of a moderately incoherent beam. In both cases they tend on propagation to approach the coherent case, in agreement with the van Cittert-Zernike theorem.

It is worth examining the moderately incoherent case, with $\delta = 8$mm, shown in Fig. 3.1(b), in more detail. For this value of the wander parameter, the beam is

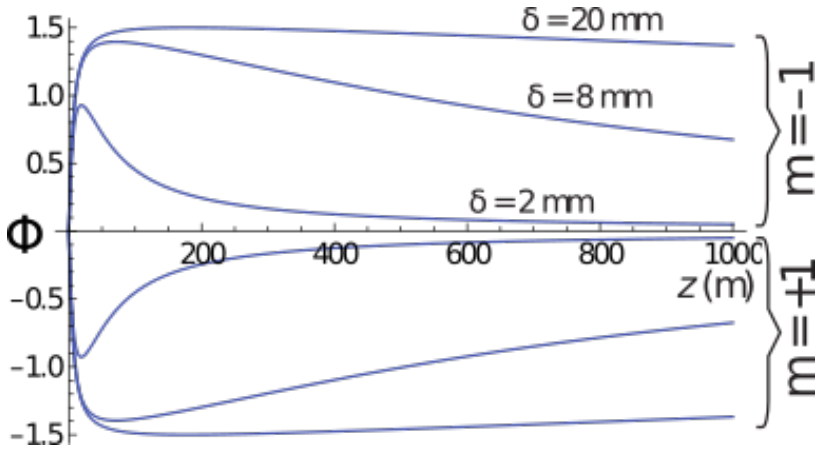

Figure 3.2: Zero manifolds of a partially coherent vortex beam on propagation. Angular positions on propagation, with $w_0 = 1$ mm, $\lambda = 500$ nm.

allowed to wander up to eight times the width of the beam at its waist, and can be considered significantly incoherent. At short propagation distances, the hyperbola very nearly meet at the $\rho_- = 0$ line, indicating that correlation singularities can be found at any radial distance from the center of the beam, provided $\rho_1 \approx \rho_2$. As the field propagates, however, the hyperbolas angle away and asymptotically approach the coherent limit. However, it can be be readily shown from Eq. (3.40) that the upper and lower branches of the hyperbola will remain separated by a distance $\Delta\rho_- = 2\delta$ for large values of z. This implies that, for a distant observation point $\boldsymbol{\rho}_1$, the field will appear to have a coherent vortex at the origin in $\boldsymbol{\rho}_2$. When $\boldsymbol{\rho}_1$ is close to the origin, however, the zero hyperbolas deviate significantly from straight line coherent case. Thus it would appear that after a lengthy propagation, there will appear a correlation vortex at the origin only if the observation point is sufficiently distant from the origin.

Also interesting is the behavior of the angular position of the singularities on propagation, as illustrated in Fig. 3.2. As the field propagates, the angle between the vectors $\boldsymbol{\rho}_+$ and $\boldsymbol{\rho}_-$ quickly diverges from $\Phi = 0$ and, for beams which are initially highly incoherent, approaches $\mp\pi/2$, corresponding to a vortex charge of $m = \pm 1$. While this "kink" in the location of the singularities does eventually return to $\Phi = 0$

as the beam propagates, highly incoherent beams may never do so in a reasonable distance. For example, at $\delta = 20$mm, we still have $\Phi = 0.1$ even at $z = 50$km.

The origin of this "kink" in the angle is a result of what may loosely be called an interaction between the phase due to the wavefront curvature $R(z)$ and the phase of the original vortex. In the waist plane and at large distances, the curvature is approximately infinite, i.e. the wavefront is planar, and the phase due to the wavefront curvature is constant. At intermediate propagation distances, however, the two phases mix to produce a charge-dependent change in the topology of the singularity. It is to be noted that this angular shift may provide a non-interferometric method for measuring the topological charge of a partially coherent vortex beam, as the charge can be determined from the location of the zeros, rather than the phase structure of the beam.

These results represent the first theoretical treatment of the full propagation characteristics of a partially coherent vortex beam. However, it only describes the first-order. Additional work is needed to describe higher-order beams.

3.3 Partially Coherent Vortex Beams of Any Order

Now that we have considered the first order PCVB's behavior on propagation and determined that correlation vortices will only occur in the same transverse plane (i.e. $z_1 = z_2 = z$), we are more ably equipped to address ourselves to the problem of the derivation of a complete class of partially coherent vortex beams of arbitrary order.

3.3.1 Derivation

As previously noted, it is mathematically convenient when working with partially coherent beams to work in the frequency domain with the cross-spectral density function $W(\mathbf{r}_1, \mathbf{r}_2, \omega)$, which we write here as

$$W(\mathbf{r}_1, \mathbf{r}_2) = \langle \tilde{U}(\mathbf{r}_1 - \mathbf{r}_0) U(\mathbf{r}_2 - \mathbf{r}_0) \rangle_\omega, \tag{3.48}$$

where $\langle ... \rangle_\omega$ again represents an average over an ensemble of monochromatic fields. We use again a tilde throughout this section to represent the complex conjugate for notational convenience, and suppress ω for brevity.

We begin our calculation with the equation for a monochromatic Laguerre-Gauss beam of radial order 0, azimuthal order $\pm m$, with $m \geq 0$, expressed as

$$U(x, y, z) = C(x \pm iy)^m \exp - \left[\frac{1}{\sigma^2}(x^2 + y^2)\right] \exp\left[-i\omega t\right], \tag{3.49}$$

where

$$C \equiv \sqrt{\frac{2}{\pi w_z^2 |m|!}} \left(\frac{\sqrt{2}}{w_z}\right)^{|m|} \exp\left[-i\Phi(z)\right], \tag{3.50}$$

and $\Phi(z)$, w_z, R_z and σ are as defined in the previous section.

In discussing correlation singularities, we will restrict ourselves to the case where $\mathbf{r}_1$ and $\mathbf{r}_2$ lie in the same transverse plane (i.e. $z_1 = z_2 \equiv z$), since it was shown in the previous section that singularities only appear in this case. We can use Eq. (3.49) to generate *mth*-order partially coherent beams by introducing it into the beam wander model discussed in Section 3.1. Thus we are able to write the cross-spectral density integral as

$$\begin{aligned} W(\mathbf{r}_1, \mathbf{r}_2) = & \\ & \frac{|C|^2}{\pi\delta^2} \int \left[(x_1 - x_0) \mp i(y_1 - y_0)\right]^m \left[(x_2 - x_0) \pm i(y_2 - y_0)\right]^m \\ & \times \exp\left\{-\frac{1}{\tilde{\sigma}^2}\left[(x_1 - x_0)^2 + (y_1 - y_0)^2\right]\right\} \\ & \times \exp\left\{-\frac{1}{\sigma^2}\left[(x_2 - x_0)^2 + (y_2 - y_0)^2\right]\right\} \\ & \times \exp\left\{-\frac{x_0^2 + y_0^2}{\delta^2}\right\} dx_0 dy_0. \end{aligned} \tag{3.51}$$

This integral can be solved analytically with careful use of the binomial theorem,

which allows us to reduce it to a sum of integrals of Gaussian form with known solutions. Those not interested in the lengthy derivation can skip to the result in Eq. (3.70). We begin by completing the square with respect to x_0 and y_0 in the exponent, introducing the quantities

$$A \equiv \frac{1}{\tilde{\sigma}^2} + \frac{1}{\sigma^2} + \frac{1}{\delta^2} = \frac{2}{w_z^2} + \frac{1}{\delta^2}, \tag{3.52}$$

$$B_x \equiv 2\left(\frac{x_1}{\tilde{\sigma}^2} + \frac{x_2}{\sigma^2}\right), \tag{3.53}$$

$$B_y \equiv 2\left(\frac{y_1}{\tilde{\sigma}^2} + \frac{y_2}{\sigma^2}\right). \tag{3.54}$$

This allows us to put the cross-spectral density into the form

$$\begin{aligned} W(\mathbf{r}_1, \mathbf{r}_2) = {} & \frac{|C|^2}{\pi\delta^2} \exp\left[B_x^2/A\right] \exp\left[B_y^2/A\right] \\ & \times \exp\left[-\frac{1}{\tilde{\sigma}^2}\left[x_1^2 + y_1^2\right]\right] \exp\left[-\frac{1}{\sigma^2}\left[x_2^2 + y_2^2\right]\right] \\ & \times \int \left[(x_1 - x_0) \mp i(y_1 - y_0)\right]^m \left[(x_2 - x_0) \pm i(y_2 - y_0)\right]^m \\ & \times \exp\left[-A(x_0 - B_x/A)^2\right] \exp\left[-A(y_0 - B_y/A)^2\right] dx_0 dy_0. \end{aligned} \tag{3.55}$$

As the exponential factors outside the integral do not significantly affect the structure of the field, we define a new function

$$\begin{aligned} D(\mathbf{r}_1, \mathbf{r}_2) \equiv {} & \frac{|C|^2}{\pi\delta^2} \exp\left[B_x^2/A\right] \exp\left[B_y^2/A\right] \\ & \times \exp\left[-\frac{1}{\tilde{\sigma}^2}\left[x_1^2 + y_1^2\right]\right] \exp\left[-\frac{1}{\sigma^2}\left[x_2^2 + y_2^2\right]\right], \end{aligned} \tag{3.56}$$

for brevity. We can now make the coordinate transformation

$$X \equiv x_0 - \frac{B_x}{2A}, \tag{3.57}$$

$$Y \equiv y_0 - \frac{B_y}{2A}, \tag{3.58}$$

and introduce

$$H_j^{\pm} \equiv x_j \pm y_j - \left(\frac{B_x}{A} \pm i \frac{B_y}{A} \right), \quad j = 1, 2. \tag{3.59}$$

We can now rewrite the integral in the relatively simple form

$$W(\mathbf{r}_1, \mathbf{r}_2) = D(\mathbf{r}_1, \mathbf{r}_2) \int \left[H_1^{\mp} - (X \mp iY) \right]^m \exp\left[-AX^2 \right] \times \left[H_2^{\pm} - (X \pm iY) \right]^m \exp\left[-AY^2 \right] dX dY. \tag{3.60}$$

This integral is still too difficult to directly integrate, but it is now possible to apply the binomial expansion twice to the integrand, so that

$$\left[H_1^{\mp} - (X \mp iY) \right]^m = \sum_{k=0}^{m} \binom{m}{k} (-H_1^{\mp})^{m-k} (X \mp iY)^k, \tag{3.61}$$

$$\left[H_2^{\pm]} - (X \pm iY) \right]^m = \sum_{l=0}^{m} \binom{m}{l} (-H_2^{\pm})^{m-l} (X \pm iY)^l. \tag{3.62}$$

We thus have

$$W(\mathbf{r}_1, \mathbf{r}_2) = D(\mathbf{r}_1, \mathbf{r}_2) \sum_{k=0}^{m} \sum_{l=0}^{m} \binom{m}{k} \binom{m}{l} \times \int (-H_1^{\mp})^{m-k} (X \mp iY)^k (-H_2^{\pm})^{m-l} (X \pm iY)^l \times \exp\left[-A(X^2 + Y^2) \right] dX dY. \tag{3.63}$$

We now note that the integrand has a rotational symmetry about the (X, Y) origin. By moving into polar coordinates such that

$$X + iY = \rho \exp[i\phi], \tag{3.64}$$

we can rewrite the cross-spectral density equation into the more easily integrable form

$$W(\mathbf{r}_1,\mathbf{r}_2) = D(\mathbf{r}_1,\mathbf{r}_2)\sum_{k=0}^{m}\sum_{l=0}^{m}\binom{m}{k}\binom{m}{l} \times (-H_1^{\mp})^{m-k}(-H_2^{\pm})^{m-l} \times \int \rho^{k+l}\exp\left[-A\rho^2\right]\exp\left[\pm i(l-k)\phi\right]\rho d\rho d\phi. \tag{3.65}$$

The integral over ϕ is equal to $2\pi\delta_{lk}$, where δ_{lk} is the Kronecker delta. Summing over l then reduces the double sum to a single sum with $l = k$. So now the cross-spectral density is reduced to

$$W(\mathbf{r}_1,\mathbf{r}_2) = 2\pi D(\mathbf{r}_1,\mathbf{r}_2)\sum_{l=0}^{m}\binom{m}{l}^2(-H_1^{\mp})^{m-l}(-H_2^{\pm})^{m-l} \times \int \rho^{2l+1}\exp\left[-A\rho^2\right]d\rho. \tag{3.66}$$

The remaining integral can be directly related to the Gamma function,

$$\Gamma(n) = (n-1)!, \tag{3.67}$$

so that

$$W(\mathbf{r}_1,\mathbf{r}_2) = 2\pi D(\mathbf{r}_1,\mathbf{r}_2)\sum_{l=0}^{m}\binom{m}{l}^2(-H_1^{\mp})^{m-l}(-H_2^{\pm})^{m-l}\frac{\Gamma(l+1)}{2A^{l+1}}, \tag{3.68}$$

where $\Gamma(l+1)$ is the Gamma function.

In this form, it is difficult to see the functional dependence, as $H_j^{\pm}$ depends on the position vectors $\mathbf{r}_1$ and $\mathbf{r}_2$. With some rearrangement however, we may readily rewrite

$$H_2^{\pm} = \left[1 - \frac{1}{\sigma^2 A}\right](x_2 \pm iy_2) - \frac{1}{\tilde{\sigma}^2 A}(x_1 \pm iy_1), \tag{3.69}$$

with a similar expression for $H_1^{\mp}$. We may finally write a complete expression for the cross-spectral density of a PCVB of any azimuthal order as

$$W(\mathbf{r}_1,\mathbf{r}_2) = \pi D(\mathbf{r}_1,\mathbf{r}_2)\Bigg\{\sum_{l=0}^{m-1}\binom{m}{l}^2\frac{\Gamma(l+1)}{A^{2m-l+1}} \times\left[\frac{1}{\tilde{\alpha}^2}(x_2\pm iy_2)-\frac{1}{\tilde{\sigma}^2}(x_1\pm iy_1)\right]^{m-l} \times\left[\frac{1}{\alpha^2}(x_1\mp iy_1)-\frac{1}{\sigma^2}(x_2\mp iy_2)\right]^{m-l} +\frac{\Gamma(m+1)}{A^{m+1}}\Bigg\}, \tag{3.70}$$

where

$$\frac{1}{\alpha^2}\equiv\frac{1}{\sigma^2}+\frac{1}{\delta^2}. \tag{3.71}$$

Equation (3.70) is the main result of this section. In it we have an analytic expression for an entire class of partially coherent vortex beams of any azimuthal order at any propagation distance.

We can make a few basic observations concerning this result. Firstly, it is a straightforward matter to show that the exponential factor $D(\mathbf{r}_1,\mathbf{r}_2)$ can be rewritten as

$$D(\mathbf{r}_1,\mathbf{r}_2)=\frac{|C|^2}{\pi\delta^2}\exp\left[-\frac{\rho_2^2}{A\sigma^2\delta^2}\right]\exp\left[-\frac{\rho_1^2}{A\tilde{\sigma}^2\delta^2}\right]\exp\left[-\frac{|\boldsymbol{\rho}_1-\boldsymbol{\rho}_2|^2}{A|\sigma|^4}\right]. \tag{3.72}$$

This indicates that the exponential factors have the form of a Gaussian Schell-model beam, discussed in Section 2.4, in which the spectral degree of coherence depends only on the difference between the two points $\mathbf{r}_1$ and $\mathbf{r}_2$. However, the cross-spectral density in its entirety is not Schell-model due to the vortex terms.

We can also find an estimate for the correlation length for the beam from this function. Looking more closely at the scaling factor $1/\Delta^2\equiv 1/A|\sigma|^4$ of Eq. (3.72)

and taking it in the $z = 0$ plane we find it takes the simple form

$$\Delta^2 = 2w_z^2 + \frac{w_z^4}{\delta^2}. \tag{3.73}$$

For sufficiently small values of δ, the correlation length is approximately $\Delta \sim w_z^2/\delta$, demonstrating the inverse relationship between beam wander and coherence.

This also highlights a limitation of the beam wander model. As $\delta \to \infty$, the correlation length reaches a minimum of $2w_z^2$. This lower limit is a result of the partially coherent field being constructed of fully coherent beams of effective width $2w_z^2$. To get a smaller correlation, one must use a smaller beam width.

3.3.2 Characteristics of PCVB singularities

We are now interested in studying how the structure of the PCVB is affected when the spatial coherence of the beam is reduced, or, equivalently, the beam allowed to wander more. Correlation vortices exist at those pairs of points $\mathbf{r}_1$ and $\mathbf{r}_2$ for which $\mathrm{Re}\{W\} = 0$ and $\mathrm{Im}\{W\} = 0$.

Due to the difficulties in visualizing the behavior of a four-dimensional correlation function, even when viewed solely in a transverse plane and not considering propagation effects, it is helpful to hold one of the position vectors constant. The phase structure of the cross-spectral density can then be plotted as function of the two variables of the remaining vector. This allows for a far easier assessment of the singularities' characteristics for a variety of conditions. It must noted that it is necessary to have the fixed point displaced from the central beam axis if vortices are to be observed. When $\mathbf{r}_1$ lies directly on axis [i.e., $(x_1, y_1) = (0, 0)$], the system is completely rotationally symmetric with respect to $\mathbf{r}_2$ and the only singularities observed are zero circles, known as ring dislocations, as seen in [33]. When $\mathbf{r}_1$ is non-zero a variety of interesting vortex structures can be observed.

3.3.3 Phase Structures of PCVBs

We begin by considering the behavior of an $m = 3$ PCVB and its associated singularities as the coherence decreases, as illustrated in Fig. 3.3. Parts (a), (c) and (e) show the color-coded phase of the correlation function as δ increases from nearly coherent to nearly incoherent. The zero lines of the real and imaginary parts of the cross-spectral density are shown in (b), (d) and (f) to more clearly demonstrate the relationship between the zeros of the function and the phase structure. For these images we have taken the fixed point to lie along the y-axis ($y = 1$ mm), while the beam's width is $w_0 = 5$ mm.

For a highly coherent beam, (a) and (b), there is effectively a single, third-order vortex at the origin, as would be expected for a fully coherent beam, with the phase increasing by 6π (i.e., $2\pi m$, with $m = 3$) as one progresses counterclockwise around the central singularity.

As the coherence decreases, (c) and (d), the central singularity separates into three first-order singularities, all evidently lying along the y-axis. The singularities align on this axis due to our choice of fixed point, which is also on the y-axis and provides the only break in rotational symmetry. This splitting of the singularity is expected, as only first-order singularities are stable under wavefield perturbations, including a decrease in coherence.

As the coherence decreases further, (e) and (f), new singularities appear, with equal and opposite signs of the original singularities, coming in from the point at infinity. As correlation vortices themselves do not possess any energy or inertia, they are able to move, in essence, "infinitely fast," coming from infinity to a finite distance with a finite change in coherence. In the low-coherence limit, the equiphase contours around each vortex compress, result in two step-like jumps of π as one goes around the vortex instead of a smooth 2π ramp.

The existence of these vortices can be deduced from Eq. (3.70), which shows

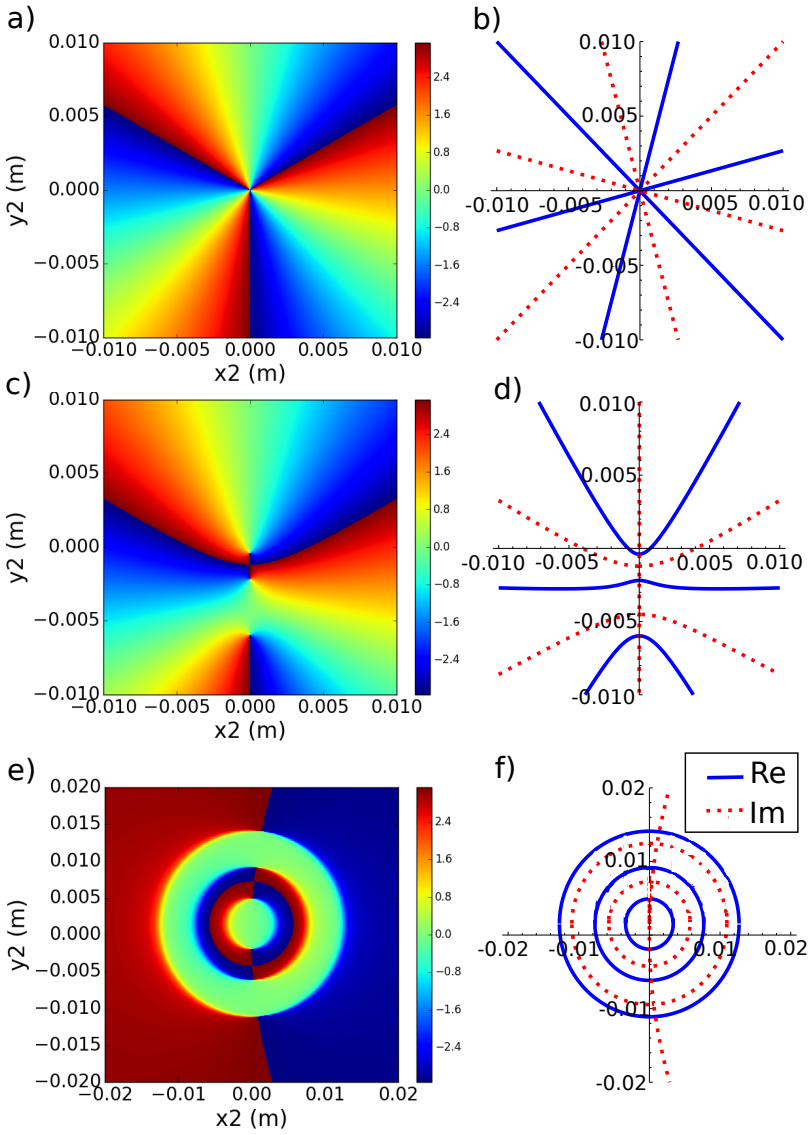

Figure 3.3: Phase of the cross-spectral density of a PCVB with m=3. For each of the images above, the beam waist $w_0 = 5$mm, $\lambda = 500$nm, $(x_1, y_1) = (0.0, .001)$m and $m = 3$. Phase plot for a beam with a) $\delta = 0.00001$m, c) $\delta = 0.001$m, e) $\delta = 0.1$m. Real and imaginary parts with locations of vortices circled for beam with b) $\delta = 0.00001$m, d) $\delta = 0.001$m, f) $\delta = 0.1$m.

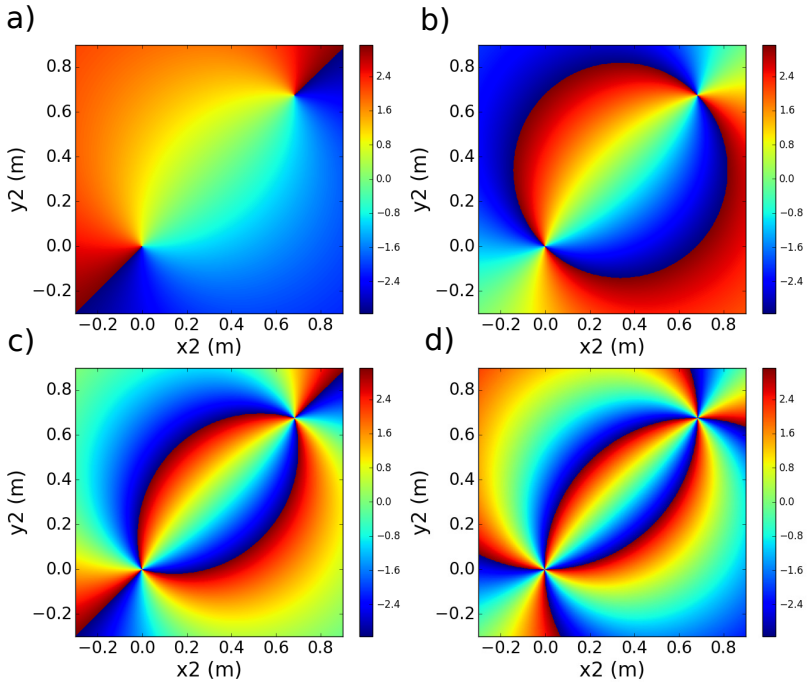

Figure 3.4: Phase of the cross-spectral density of a PCVB of different vortex orders. For each of the images above, the beam waist $w_0 = 5$mm, $\lambda = 500$nm, $(x_1, y_1) = (.001, .001)$m, and $\delta = .001$m. a) $m = 1$ b) $m = 2$ c) $m = 3$ d) $m = 4$. The pairs of clockwise and anticlockwise vortices can be seen along the line $x = y$ bisecting the elliptical structure. For every increase in order, another pair is formed.

that the cross-spectral density contains a $2m$th-order polynomial in $z_2 = x_2 + iy_2$. Alternately, this can be thought of as an mth-order polynomial in z_2 and an mth-order polynomial in $\tilde{z}_2$. Thus we expect $2m$ distinct roots for this polynomial, which would suggest $2m$ vortices, divided equally between left- and right-handed vortices.

A feature of particular interest that can be seen in Fig. 3.3(f) is that the vortices in fact do not lie along a straight line, but instead lie on circles formed by the circular form of the imaginary and real zeros of the cross-spectral density. This is distinct from the $m = 1$ case, discussed in Ref. [44], where it was shown that for the waist plane of the beam the two correlation vortices lie along a straight line which intersects the origin. It can be shown from Eq. (3.70) that this is approximately true for the $|m| > 1$ case only when the field is highly coherent. The circles associated with the zeros of the real part of the cross-spectral density can be found by taking the limit as $\delta \to \infty$ in Eq. (3.70). We then arrive at an expression for the cross-spectral density of

$$W(\mathbf{r}_1, \mathbf{r}_2) = \pi D(\mathbf{r}_1, \mathbf{r}_2) \frac{w_z^{2m+2}}{2^{m+1}} \Bigg\{ \sum_{l=0}^{m-1} \binom{m}{l} \Gamma(l+1) \times (-1)^{m-l} |z_2 - z_1|^{2(m-l)} + \Gamma(m+1) \Bigg\}, \tag{3.74}$$

where we have used $z_1 = x_1 \pm iy_1$, etc. This expression is completely real-valued, and is a $2m$th-order polynomial in $|z_2 - z_1|$, indicating that the $2m$ zeros of the real part of $W(\mathbf{r}_1, \mathbf{r}_2)$, with respect to $\mathbf{r}_2$, lie on circles centered on $\mathbf{r}_1$.

The approximate zeros of the imaginary part of $W(\mathbf{r}_1, \mathbf{r}_2)$ come from returning to Eq. (3.70) and keeping the lowest order terms with respect to $1/\delta^2$. The condition for the imaginary part of $W(\mathbf{r}_1, \mathbf{r}_2)$ to vanish is then

$$\frac{y_1}{x_1} = \frac{y_2}{x_2}, \tag{3.75}$$

or approximately a line passing through the origin and $\mathbf{r}$. We note here that the circles of Eq. (3.74) have finite radii as $\delta \to \infty$; we interpret this as a consequence of the fact that the correlation length of the field never approaches zero, as indicated by Eq. (3.73). This suggests that a more advanced model will be necessary to study partially coherent vortex beams in the low coherence limit. We also note that the position of the vortices changes in a non-trivial manner as the field propagates, as was discussed for the $m = 1$ case in Ref. [44] and in Section 3.2.2.

The equal and opposite sets of vortices can be seen for different values of m in Fig. 3.4. Now the fixed point has been placed on the diagonal, and all zeros consequently lie along a diagonal line running through the origin. In this zoomed out cross-section of the beam, the individual groups of positive and negative vortices appear as a single high-order vortex, though in fact they are closely spaced sets of first-order vortices.

It is to be noted again that it is necessary to have the fixed point displaced from the central beam axis if the vortices are to be observed. When $\mathbf{r}_1$ lies directly on axis, the system is completely rotationally symmetric with respect to $\mathbf{r}_2$ and the only singularities observed are ring dislocations as seen in Ref. [32].

3.3.3.1 Topological Charge of PCVBs

As already seen in previous examples, the phase always changes by an integer multiple of 2π when one follows a closed counterclockwise trajectory around a vortex; this integer is known as the topological charge. It can be shown that the net topological charge of a vortex beam is in general conserved, and typically vortices only appear or disappear in pairs of equal and opposite charge that conserves the net charge. These properties of vortices, discreteness and stability, make them of interest for free-space optical communications, because they indicate that a vortex might be a turbulence-resistant carrier of information [51]. However, it is important to understand what effect decreasing coherence has on the detectable topological charge of a PCVB; here we quantify this relationship.

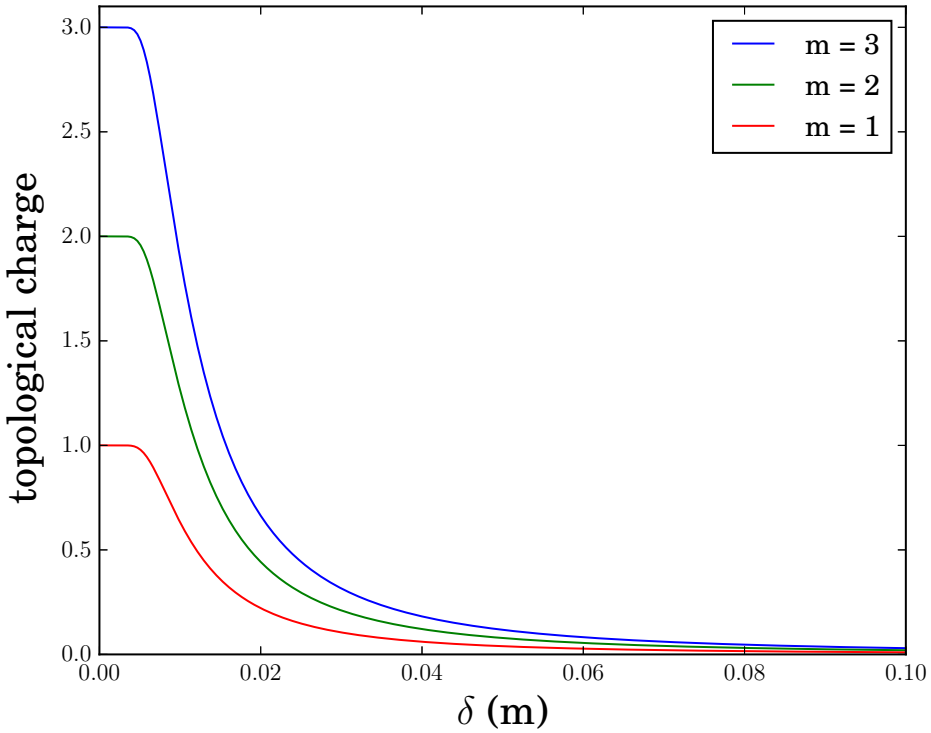

Figure 3.5: Topological charge of a PCVB as a function of δ as expressed in Eq. 3.76, showing the gradual loss of charge as beam wander is increased. The detector radius is $a = 1$ cm.

It is to be noted that there are several possible ways to measure the topological charge of the PCVBs; we consider two here. Provided the field fluctuations are slow enough, the instantaneous topological charge within an aperture can be measured and the average value calculated. Using the beam wander model, the measured topological charge will be m if $\mathbf{r}_0$ lies within a circular aperture A of radius a, and 0 if $\mathbf{r}_0$ lies outside the aperture. The average topological charge $\bar{t}$ of a beam will be given by

$$\bar{t} = m \int_A f(\mathbf{r}_0) d^2\mathbf{r}_0 = m[1 - \exp(-a^2/\delta^2)]. \tag{3.76}$$

If $\delta = 0$, $\bar{t} = m$ and if $\delta \to \infty$, $\bar{t} \to 0$, as can be seen in Figure 3.5.

That being said, we typically might expect the fluctuations of the field to be too

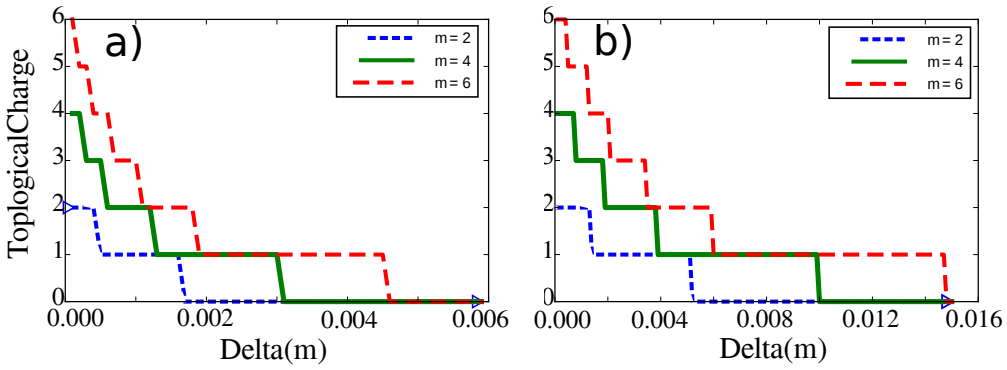

Figure 3.6: Topological charge of a PCVB as a function of beam wander. The beam waist $w_0 = 5$mm, and $\lambda = 500$nm The detector radius was set at 1cm. As δ increases, the coherence of the beam decreases, and the detectable topological charge drops. a) $(x_1, y_1) = (.0001, .0001)$m b) $(x_1, y_1) = (.001, .001)$m. Shifting the fixed point farther away from the origin has the same effect as increasing the coherence.

fast to directly measure; in such a situation, we can only measure the topological charge of the cross-spectral density. To do so, one must choose a fixed point $\mathbf{r}_1$ and determine the charge with respect to the point $\mathbf{r}_2$. This can only be accomplished using interferometry.

Figure 3.6 shows the topological charge of PCVBs of three different orders as a function of δ. The topological charge is calculated within a circular aperture of radius 1 cm. The point $\mathbf{r}_1$ must again be fixed for the calculation, and the loss of charge is shown for two different positions of this fixed point in (a) and (b). It can be seen that as δ increases, and coherence therefore decreases, the topological charge is lost in discrete drops. Evidently the charge is more robust for a fixed point further away from the origin, but it is still lost for a wander parameter δ significantly smaller than the aperture size. Higher-order beams maintain some amount of charge longer than lower-order beams, while lower order beams maintain their initial charge value for larger values of δ.

This result suggests that the use of vortices and partial coherence together in any application will naturally involve a trade-off. Though partially coherent beams typically propagate through the atmosphere with smaller intensity fluctuations than

their fully coherent counterparts, these beams will also typically start out with a topological charge reduced from the fully coherent case. The optimal balance of vortex and coherence properties will depend on the specifics of the application.

We have already seen that this loss of topological charge can be attributed to the appearance of oppositely-charged vortices from infinity. An alternative way to explain the effect, perhaps more readily understandable, is to return to the beam wander model. As the coherence is decreased, and the beam is allowed to wander more from the central axis, it will spend more time with its vortex lying outside of the region of the aperture, and undetectable. One would expect that the average topological charge would therefore also be reduced.

3.3.4 Orbital Angular Momentum

It has long been known [52] that a vortex structure in an optical beam can be connected to the orbital angular momentum (OAM) of the beam, and it is therefore of interest to study how the OAM of PCVBs depend on the state of coherence.

The quantity of interest is the z-component of the orbital angular momentum flux density flowing across a plane of constant z, which represents the flux density of OAM as a function of position in the cross section of the beam. For a partially coherent, electromagnetic field this flux density may be expressed as [35][2]

$$L_{orbit}(\mathbf{r},\mathbf{r}',\omega) = \frac{-\epsilon_0}{2k}\,\mathrm{Im}\Big\{ y\frac{\partial'}{\partial x_1}W_{yy}(\mathbf{r},\mathbf{r}',\omega) - x\frac{\partial'}{\partial y}W_{yy}(\mathbf{r},\mathbf{r}',\omega) - x\frac{\partial'}{\partial y}W_{xx}(\mathbf{r},\mathbf{r}',\omega) + y\frac{\partial'}{\partial x}W_{xx}(\mathbf{r},\mathbf{r}',\omega)\Big\}_{\mathbf{r}=\mathbf{r}'} \tag{3.77}$$

where W_{yy}, W_{xx} represent the diagonal elements of the cross-correlation tensor. For an unpolarized beam,$W_{xx} = W_{yy} = W$, and the expression simplifies to

$$L_{orbit}(\mathbf{r},\omega) = \frac{-\epsilon_0}{k}\,\mathrm{Im}\left\{ y\frac{\partial'}{\partial x_1}W(\mathbf{r},\mathbf{r}',\omega) - x\frac{\partial'}{\partial y_1}W(\mathbf{r},\mathbf{r}',\omega)\right\}_{\mathbf{r}=\mathbf{r}'}. \tag{3.78}$$

[2]The analogous expression in Ref. [35] contained a sign error that has been corrected here.

On substitution from Eq. 3.70 into 3.78, we have

$$L_{orbit}(\mathbf{r},\omega) = \beta\frac{\pi\epsilon_0}{k}\exp[-2r^2/w_z^2\beta]\sum_n^m C_n^m(m-n)r^{2(m-n)}, \tag{3.79}$$

where

$$C_n^m \equiv \binom{m}{n}^2 \frac{|c|^2}{\pi\delta^2}\frac{\Gamma(n+1)}{A^{(n+1)}}\beta^{-2(m-n)}, \tag{3.80}$$

$$\beta \equiv \left(1+\frac{2\delta^2}{w_z^2}\right), \tag{3.81}$$

and $r = \sqrt{x^2+y^2}$.

This unnormalized quantity depends on both the intensity of the beam and the density of the angular momentum. We define a normalized angular momentum flux density, which may be roughly understood as the orbital angular momentum density per photon of a vortex beam as a function of radial position,

$$l_{orb}(\mathbf{r},\omega) = \frac{\hbar\omega L_{orbit}(\mathbf{r},\omega)}{S(\mathbf{r},\omega)}, \tag{3.82}$$

where $S(\mathbf{r},\omega)$ is the z-component of the Poynting vector,

$$S(\mathbf{r},\omega) = \frac{k}{\mu_0\omega}W(\mathbf{r},\mathbf{r},\omega) \tag{3.83}$$

$$= \frac{\pi k}{\mu_0\omega}\exp[-2r^2/w_z^2\beta]\sum_{n=0}^m C_n^m r^{2(m-n)}. \tag{3.84}$$

With a small amount of effort, the normalized OAM flux density can be shown to have the form

$$l_{orb}(r,\omega) = \hbar\beta\frac{\sum_{n=0}^{m-1} C_n^m(m-n)r^{2(m-n)}}{\sum_{n=0}^{m-1} C_n^m r^{2(m-n)} + C_m^m}. \tag{3.85}$$

From this expression, the behavior of the OAM density as a function of vortex order may be evaluated. For small values of r, the expression takes on the approximate form

$$l_{orb}(r,\omega) \approx \hbar \left(1 + \frac{2\delta^2}{w_z^2}\right) \frac{C_{m-1}^m r^2}{C_m^m} \tag{3.86}$$

which is quadratic in r, while for larger values of r the effect of C_n^m in the denominator of Eq. (3.85) is negligible and the value approaches a constant of

$$l_{orb}(r,\omega) \approx m\hbar \left(1 + \frac{2\delta^2}{w_z^2}\right). \tag{3.87}$$

Taken together, these features describe a Rankine vortex, already observed for the first order in [53, 35]. This type of vortex can be seen in tropical cyclones [39, Section 9.8], where the wind speeds in the core increase linearly with radius and fall off inversely with the radius outside the core. The eye wall therefore rotates in a rigid fashion, while the spiral arms rotate in a fluid manner. There are several features of interest here. As can be seen from the equation or in Figure 3.7, the value of the OAM at large r increases by integer multiples of the OAM of a first order ($m = 1$) beam. Additionally, the degree of coherence has a substantial effect on how rapidly the vortex behavior shifts from rigid body-like rotation in the interior to fluid-like rotation at large r. For high coherence beams, this transition is abrupt and occurs near the edge of the beam waist (w_z). For lower coherence beams, the transition is very gradual and occurs at multiple beam waist lengths, while asymptotically approaching the same constant value as a more coherent beam.

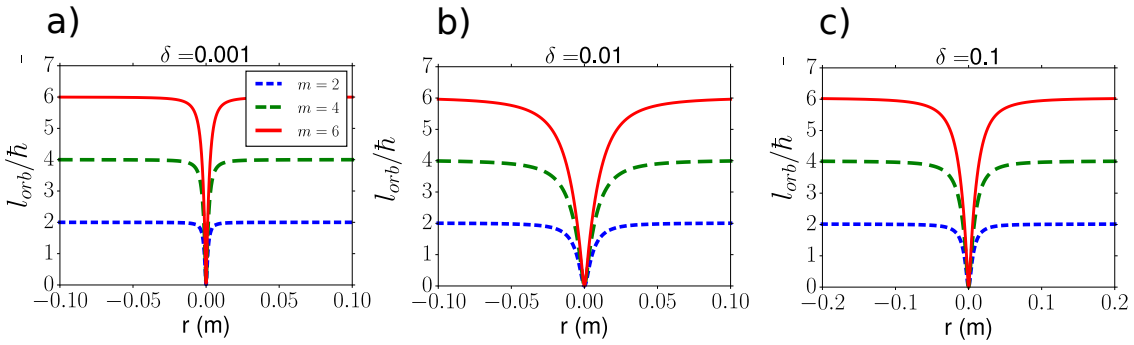

Figure 3.7: Normalized orbital angular momentum flux density for different states of coherence. For each of the images above, the beam waist $w_0 = 5$mm, $\lambda = 500$nm, and $r_1 = r_2$. a) $\delta = 0.001$m b) $\delta = 0.01$m c) $\delta = 0.1$m. Note that this is plotted on a larger range to make clear the asymptotic behavior.

CHAPTER 4: DIFFRACTION THROUGH A TRIANGULAR APERTURE

It is one thing to create a vortex, but it another thing to detect it. In the previous chapter we described a new class of partially coherent vortex beams. This chapter focuses on the diffraction of coherent vortex beams through a triangular aperture as a measurement technique for the charge of vortex beams. Portions of this chapter have been previously published [54].

4.1 Background

As has been previously mentioned, optical vortices are stable topological features of a wavefield, and are well known to be resistant to perturbations of both amplitude and phase, such as occur in propagation through a turbulent atmosphere [51] or even partial obstruction by objects [55]. This is particularly interesting because of the associated discrete topological charge of the vortex beams, which we have seen is defined as the number of cycles which the phase $\psi(\mathbf{r})$ of the field increases around a closed path C with the singularity contained within, i.e. in integral form

$$m \equiv \frac{1}{2\pi} \oint_C \nabla\psi(\mathbf{r}) \cdot d\mathbf{r}. \tag{4.1}$$

This charge must be an integer value due to the continuity of the wavefield, which makes it potentially very useful as an information carrier, particularly when the stability of vortex beams is also considered. However, because the charge is contained in the phase of the field, new techniques are necessary to detect the charge in a manner that is both reliable and efficient. One method that has shown promise is diffraction through a triangular aperture [56, 57], which is particularly appealing due to its simplicity and straightforward interpretation. A vortex beam topological charge m will

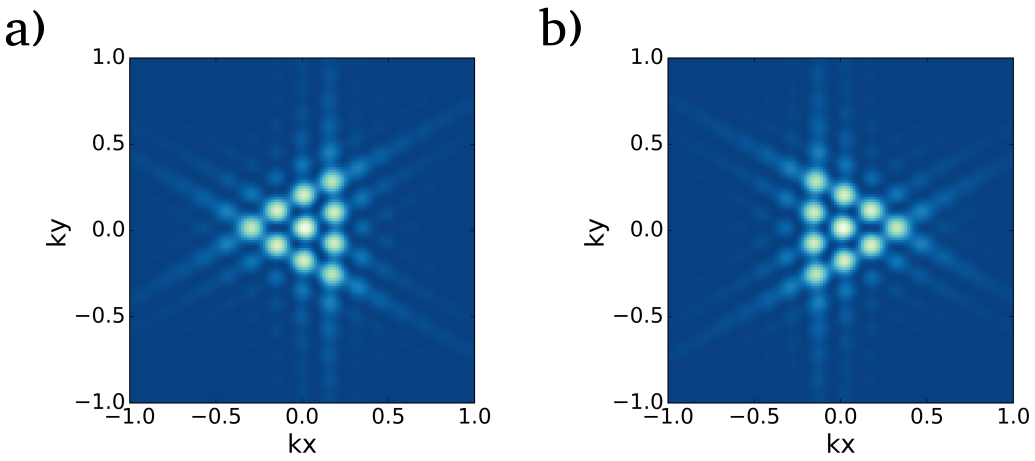

Figure 4.1: Example of diffraction through a triangular aperture, done with the FFT method, for a) $m = 3$ b) $m = -3$, with $a = 4\lambda$, $w_0 = 2a$.

produce a diffraction pattern with $m + 1$ bright spots on a side, and the orientation of the array indicates the sign of the charge, as seen in Fig 4.1. This method works for both narrow band and pulsed beams [58], and has been used to help analyze the creation of new vortices in a "fractional vortex beam" [59].

However, despite its experimental simplicity and usefulness, previous theoretical explorations of this effect have relied on direct numerical integration or have ignored the amplitude of the field in the calculation. In addition, they have focused only on the most idealized situation, which is to say a single beam centered on axis. There have to date been no explorations of non-ideal cases, e.g. off-axis diffraction or mixed charge beams, with the exception of the fractional vortex case previously mentioned. The usefulness of this detection method in real world applications such as the aforementioned free space communication depend on its behavior in such non-ideal circumstances. For instance, turbulence can cause beams to wander and their modes to scramble. A detection method that can account for this degradation would be especially useful.

In this chapter we present an analytic derivation of the diffraction of a vortex beam through a triangular aperture, taking into account its intensity as well as its phase

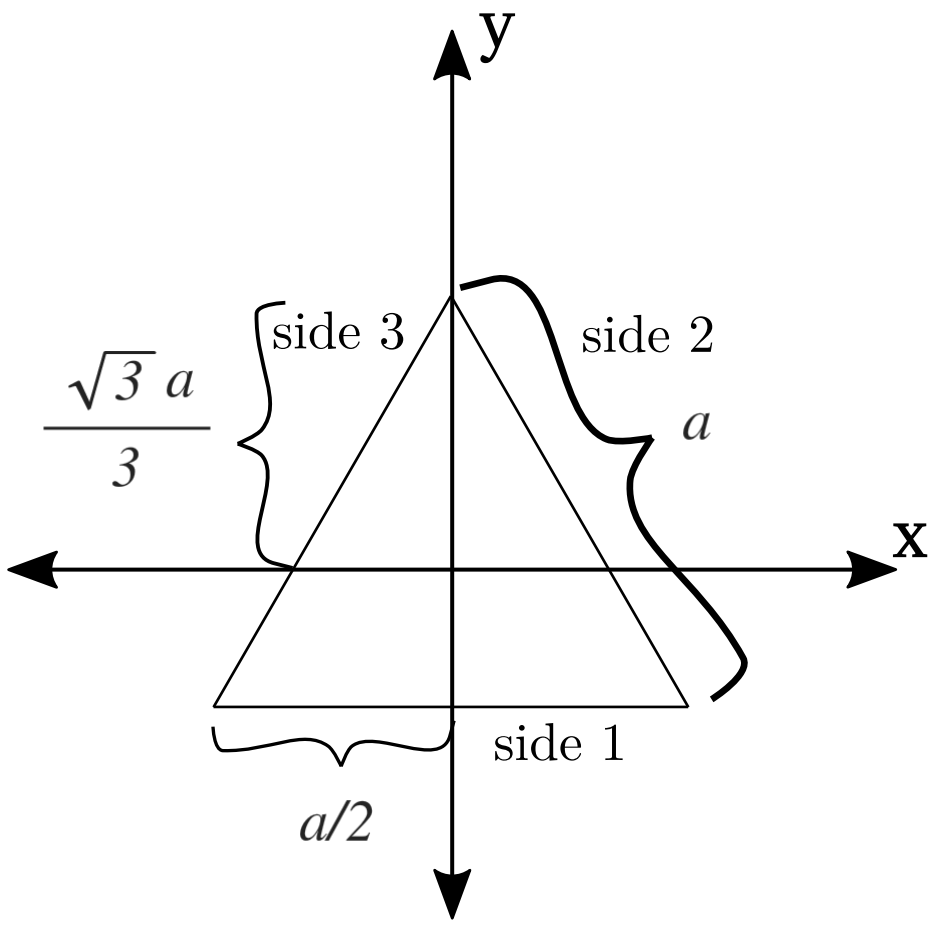

Figure 4.2: Diagram of the triangular aperture, side length a centered on the origin.

and allowing for the core of the beam to be off center of the aperture or allowing the beam to be a superposition of modes. The previous theoretical treatments cannot easily account for either off-axis beam or multi-mode. We compare our results to those produced by exact numerical simulation, and discuss those results in the context of vortex detection. Additionally, we show how our results can be extended to diffraction of a vortex by any polygonal aperture.

4.2 Derivation

We begin by considering the geometry illustrated in Fig 4.2. A Laguerre-Gauss vortex beam (LGVB) is diffracted through the triangular aperture illustrated. The aperture is centered on the origin with side length a which is smaller than the width of the beam w_0, while the core of the LGVB can be off-set from the origin to the

point (x_0, y_0). Assuming that the aperture opening is significantly smaller than the width of the beam, we can neglect the Gaussian envelope of the beam, and thus in the aperture plane the beam has the form

$$U_{\pm m}(x, y) = \frac{[(x - x_0) \pm i(y - y_0)]^m}{w_0^m}. \tag{4.2}$$

Furthermore, since the aperture side length is greater than the wavelength, we will initially treat the diffraction through the aperture as primarily an edge effect. Treating this type of superwavelength aperture diffraction with a geometrical theory of diffraction is well established [60] and is indeed employed in previous phase only investigations of the phenomenon. However, unlike previous calculations, we explicitly include the amplitude in the integration. Thus the total diffracted field may be written as

$$U(k_x, k_y) \sim \oint_C \frac{[(x - x_0) \pm i(y - y_0)]^m}{w_0^m} \exp\left[-i(k_x x + k_y y)\right] dl', \tag{4.3}$$

where C represents the boundary of the triangle, dl' is the infinitesimal path element and (k_x, k_y) is the transverse wavenumber, i.e. $k^2 = k_x^2 + k_y^2 + k_z^2$. In accordance with the Fraunhoffer diffraction theory, this diffracted field may be interpreted as either the field in the far-zone of the aperture or the field in the rear focal plane of a $2f$ focusing system, with the aperture in the front focal plane; we leave off any scaling factors in the integral associated with either specific case.

The integral along each leg of the triangle may be expressed by a linear parameterization:

$$x = a[\alpha_x t + \beta_x], \quad y = a[\alpha_y t + \beta_y], \tag{4.4}$$

with $-1/2 \leq t \leq 1/2$. The constants α_i and β_i are coefficients of the parameterization.

Table 4.1: Coefficients of Parameterization for Each Side of the Triangle

Side	$\boldsymbol{\alpha_x}$	$\boldsymbol{\beta_x}$	$\boldsymbol{\alpha_y}$	$\boldsymbol{\beta_y}$
1	1	0	0	$-\sqrt{3}/6$
2	-1/2	1/4	$\sqrt{3}/2$	$\sqrt{3}/12$
3	-1/2	-1/4	$-\sqrt{3}/2$	$\sqrt{3}/12$

Their values for the triangular case are given in Table 4.1. However, they can also be found for an aperture of arbitrary shape with some effort. The parameterization coefficients for a pentagon can be found in Appendix A along with a sample plot. Our diffraction integral for a single side is thus

$$U(k_x, k_y) \sim \gamma \exp\left[-i\chi a\right] \int_{-1/2}^{1/2} \frac{\left[a\alpha t + (a\beta - z_0)\right]^m}{w_0^m} \exp\left[-i\kappa a t\right] dt, \tag{4.5}$$

with

$$\begin{aligned} \alpha &\equiv \alpha_x \pm i\alpha_y, \\ \beta &\equiv \beta_x \pm i\beta_y, \\ \gamma &\equiv a|\alpha|, \end{aligned}$$

and

$$\begin{aligned} \chi &\equiv k_x\beta_x + k_y\beta_y = \boldsymbol{k}\cdot\boldsymbol{\beta}, \\ \kappa &\equiv k_x\alpha_x + k_y\alpha_y = \boldsymbol{k}\cdot\boldsymbol{\alpha}, \\ z_0 &\equiv x_o \pm iy_0. \end{aligned} \tag{4.6}$$

Although this notation appears somewhat verbose, it allows us to evaluate all three (or, in general, n) sides with a single form.

To begin performing the integral, we expand the vortex field into a finite series

using the binomial expansion so that

$$[a\alpha t + (a\beta - z_0)]^m = \sum_{n=0}^{m} \frac{m!}{n!(m-n)!}(a\alpha t)^n (a\beta - z_0)^{m-n}. \tag{4.7}$$

This allows us to write the integral as

$$\begin{aligned} U(k_x, k_y) \sim & \gamma \frac{\exp\left[-i\chi a\right]}{w_0^m} \sum_{n=0}^{m} \frac{m!}{n!(m-n)!}(a\alpha t)^n (a\beta - z_0)^{m-n} \\ & \times \int_{-1/2}^{1/2} t^n \exp\left[-i\kappa a t\right] dt. \end{aligned} \tag{4.8}$$

The remaining integrals can now be found using the identity

$$\int t^n \exp\left[ct\right] dt = \frac{d^n}{dc^n} \int \exp\left[ct\right] dt, \tag{4.9}$$

which, by letting $c = -i\kappa a$, gives us

$$\int_{-1/2}^{1/2} t^n \exp\left[-i\kappa a t\right] dt = \left(\frac{i}{\kappa}\right)^n \frac{d^n}{da^n} j_0\left(\frac{\kappa a}{2}\right), \tag{4.10}$$

where $j_0(x)$ is the zeroth-order spherical Bessel function

$$j_0(x) = \frac{\sin(x)}{x}. \tag{4.11}$$

For notational brevity let us define a new function

$$f_n(\kappa, a) = \left(\frac{i}{\kappa}\right)^n \frac{d^n}{da^n} j_0\left(\frac{\kappa a}{2}\right), \tag{4.12}$$

which allows us to write

$$U(k_x, k_y) \sim \gamma \frac{\exp\left[-i\chi a\right]}{w_0^m} \sum_{n=0}^{m} \frac{m!}{n!(m-n)!}(a\alpha t)^n (a\beta - z_0)^{m-n} (a\alpha)^n f_n(\kappa, a). \tag{4.13}$$

This equation, along with the parameterizations, gives us an approximate analytic expression for the diffraction of a vortex of arbitrary order and center position through one side of a polygonal aperture.Combining expressions for all edges of the aperture, it can be used to quickly evaluate the diffraction patterns of any number of vortex beams simultaneously superimposed with arbitrary positions relative to the axis. That is, a beam of order n can in general be expressed as the sum of n fields in the form of Eq. (4.13). However, with a little extra rearrangement, additional insight into the overall structure of the diffraction pattern may be obtained. This may be accomplished by employing the generalized Leibniz rule, i.e.

$$\frac{d^m}{du^m}\left[f(u)g(u)\right] = \sum_{n=0}^{m} \frac{m!}{n!(m-n)!} \frac{d^n[f(u)]}{du^n} \frac{d^{m-n}[g(u)]}{du^{m-n}}. \tag{4.14}$$

In order to apply this rule we must first effect a change in the variable of differentiation so that

$$f_n(\kappa, a) = \frac{1}{(a\alpha)^n}\left[\frac{d}{d(-i\kappa/\alpha)}\right]^n j_o(\kappa a/2). \tag{4.15}$$

Upon substitution into Eq. (4.13), the expression becomes

$$U(k_x, k_y) \sim \frac{\gamma \exp\left[-i\chi a\right]}{w_0^m} \sum_{n=0}^{m} \frac{m!}{n!(m-n)!}\left[\frac{d}{d(-i\kappa/\alpha)}\right]^n j_o(\kappa a/2). \tag{4.16}$$

Additionally, we note that

$$(a\beta - z_0)^{m-n} = \exp\left[i\kappa(a\beta - z_0)/\alpha\right]\left[\frac{d}{d(-i\kappa/\alpha)}\right]^{m-n} \exp\left[-i\kappa(a\beta - z_0)/\alpha\right]. \tag{4.17}$$

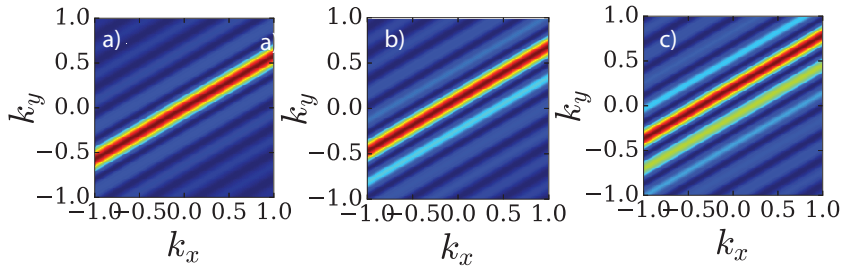

Figure 4.3: Bright diffraction lines produced by the second side of the triangular aperture, for (a) $m = 0$ (b) $m = 1$ (c) $m = 2$. We have used $a = 4\lambda$, $w_0 = 2a$.

Using this substitution, we may apply the Leibniz rule and write

$$U(k_x, k_y) \sim \frac{\gamma \exp\left[-i\chi a\right]}{w_0^m} \exp\left[i\kappa(a\beta - z_0)/\alpha\right] (i\alpha)^m \left[\frac{d}{d\kappa}\right]^m \times \left\{\exp\left[-i\kappa(a\beta - z_0)/\alpha\right] j_0(\kappa a/2)\right\}. \tag{4.18}$$

In this we have a concise expression for the diffraction of a vortex by a single edge of triangular aperture and one that gives immediate insight into the origin of the m-lobed triangular diffraction pattern that appears for a vortex of order m. Each edge will produce a diffraction pattern parallel to α as $\kappa = \boldsymbol{k} \cdot \boldsymbol{\alpha}$. For the $m = 0$ case, the largest value of $U(k_x, k_y)$ will be at the origin of the function $j_0(\kappa a/2)$. This produces a bright line perpendicular to α centered at the origin of the diffraction plane, shown in Figure 4.3a. In the $m = 1$ case, the largest values of $U(k_x, k_y)$ will be the largest values of $d[j_0(\kappa a/2)]/d\kappa$, which will be two lines corresponding with the slopes of the central peak of $j_0(\kappa a/2)$; this is illustrated in Figure 4.3b. Each higher derivative of $j_0(\kappa a/2)$ will introduce another bright line to the diffraction pattern; the $m = 2$ case is shown in Figure 4.3c.

Equation (4.18) also suggests a way to roughly estimate how far the vortex core may be displaced before the diffraction pattern is significantly affected. We begin with the observation that the peaks of the diffraction pattern will for lower orders

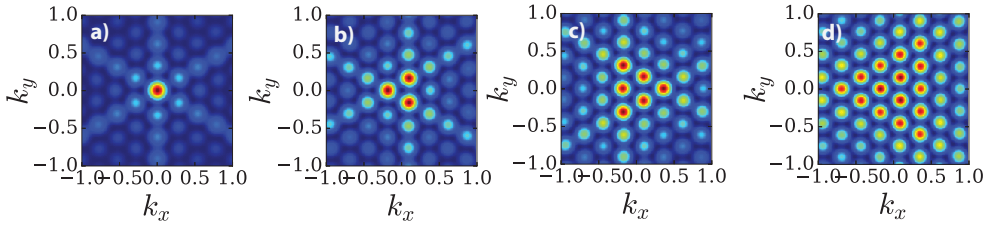

Figure 4.4: Diffraction pattern for various vortex orders, with (a) $m = 0$, (b) $m = 1$, (c) $m = -2$, (d) $m = 4$. We have used $a = 4\lambda$ and $w_0 = 2a$.

be bounded by the first zero of the zeroth order spherical Bessel function, located at $\kappa a = \pi$; we thus restrict ourselves to this relationship. We now note that the components of the complex exponential will have a small influence provided that

$$\left|\frac{\kappa z_0}{\alpha}\right| < 1. \tag{4.19}$$

Thus we find the condition on z_0 after substituting the value of κa into this expression to be

$$\left|\frac{z_0}{a}\right| < \frac{|\alpha|}{\pi} = \frac{1}{\pi}, \tag{4.20}$$

so we can expect that the off axis effects will become detrimental when $[z_0/a] \sim 0.318$.

We now return to our primary result (Eq 4.13) and use it to explore the diffraction patterns of various vortex beam configurations for vortex beams diffracted by a triangular aperture. First, we plot the familiar on axis case where $z_0 = 0$. As seen in Figure 4.4, we have reproduced the experimental results and the expected result of the $m + 1$ lobed triangle as the most prominent feature of the diffraction pattern and that the orientation depends on the sign of the charge.

Next to be considered is the case where $z_0 \neq 0$, i.e. where the vortex core is shifted relative to the center of the aperture. Figure 4.5 shows the evolution of the diffraction pattern when the core is shifted vertically. The leftmost spot gradually dims while

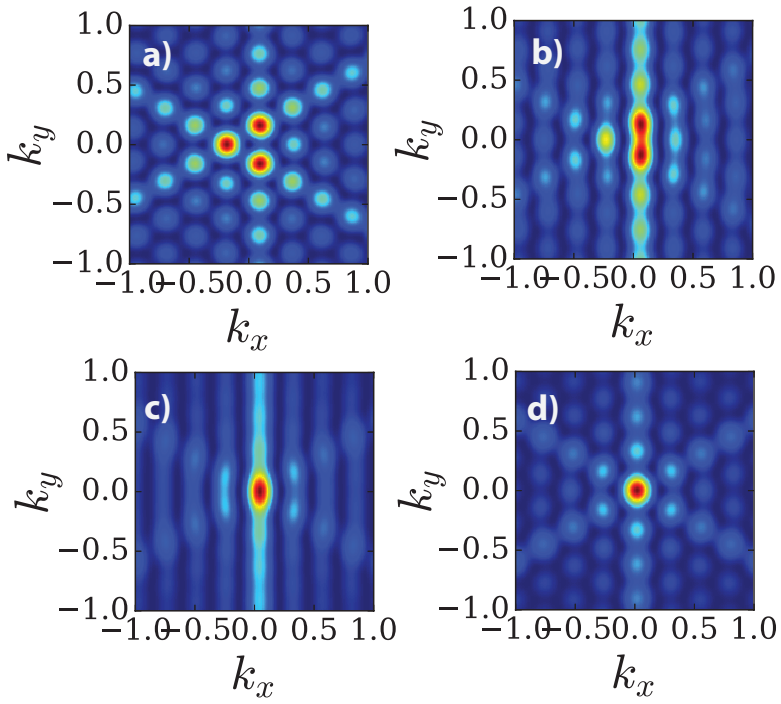

Figure 4.5: Diffraction pattern for an $m = 1$ vortex, with $x_0 = 0$ and (a) $y_0 = 0$ (b) $y_0 = 0.318a$ (c) $y_0 = 0.636a$ (d) $y_0 = 2a$. We have used $a = 4\lambda$, $w_0 = 2a$.

the intensities of the rightmost spots gradually increase until they merge together into an oblong intensity spot. As suggested in the previous section, $y_0 = 0.318a$ seems to be a rough threshold for where the distinctiveness of the diffraction pattern begins to disintegrate. Beyond that point the triangle is no longer visible. When the vortex core is moved entirely outside the aperture, the diffraction pattern mimics the $m = 0$ case. This is the expected result because the field within the aperture in such a case is effectively a tilted plane wave.

A horizontally displaced vortex core will display similar behavior on diffraction. As seen in Figure 4.6 the lower bright intensity spot transforms into the single intensity spot once the vortex center passes outside of the critical region.

The evolution of the three-lobed direction pattern to the single-lobed pattern depends entirely on the direction of the core displacement. This suggests that the

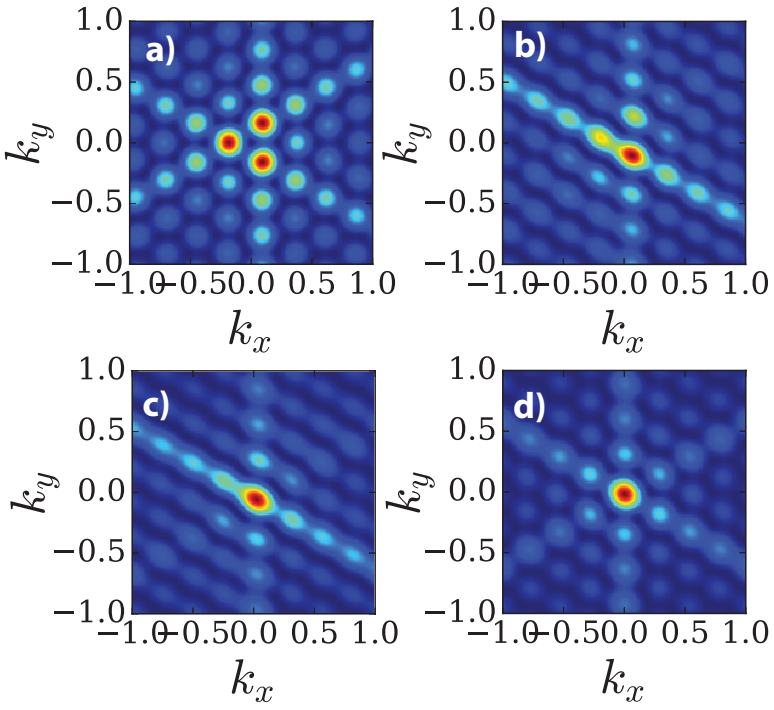

Figure 4.6: Diffraction pattern for an $m = 1$ vortex, with $y_0 = 0$ and (a) $x_0 = 0$ (b) $x_0 = 0.318a$ (c) $x_0 = 0.636a$ (d) $x_0 = 2a$. We have again used $a = 4\lambda$, $w_0 = 2a$.

changes in the intensity pattern could be used to determine, and correct for the displacement of the vortex beam. This ability may be useful in free-space optical communications, where atmospheric turbulence tends to introduce wandering of an optical beam and any vortices within it.

We may also use our analytic model to investigate the diffraction pattern of a coherent superposition of modes. Such cases are of interest for two reasons: (1) multimode vortex beams have been proposed as a way to multiplex information in free-space communication, (2) propagation through atmospheric turbulence tends to induce mode mixing even for beam which are initially single mode. We consider as an example the particular case in which we superimpose an $m = 0$ mode with an $m = 1$

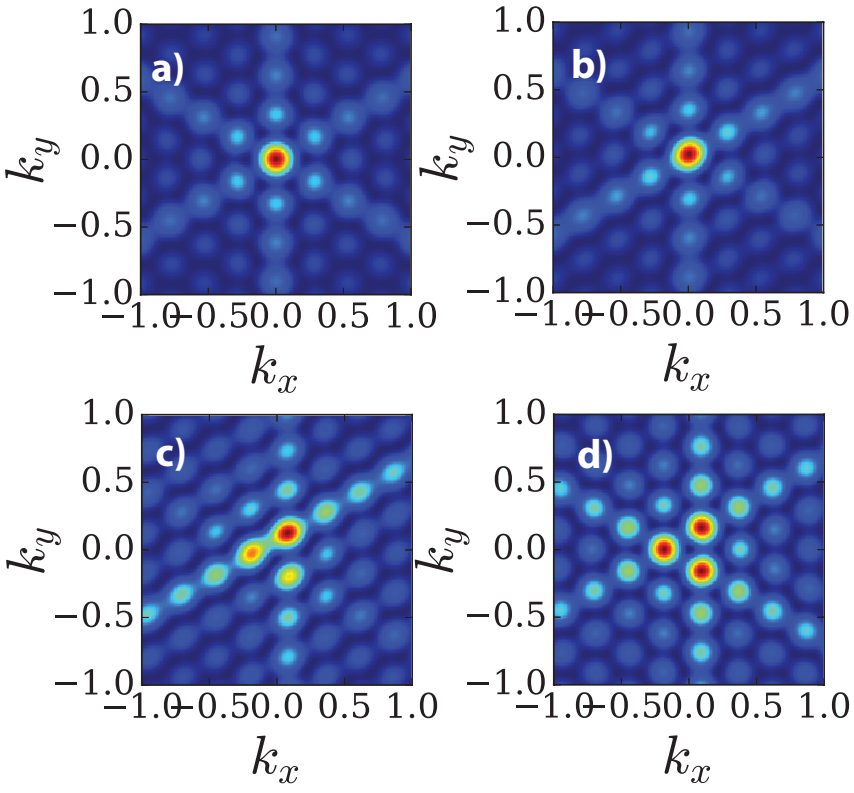

Figure 4.7: Diffraction pattern for mixed-mode beam, with (a) $b = 0$ (b) $b = 0.5$ (c) $b = .9$ (d) $b = 1.0$ We have again used $a = 4\lambda$, $w_0 = 2a$.

mode in the form

$$U(x, y) = (1 - b)U_0(x, y) + bU_1(x, y), \tag{4.21}$$

with b a real-valued weighting parameter. The results of the calculation are shown in Figure 4.7. It can be seen that the lower-order mode dominates the diffraction pattern until the amplitude of the higher-order mode is quite large, $b = 0.9$. On reflection, this is understandable because the higher-order modes naturally have a smaller intensity near their central axis, resulting in them being dominated by lower-order modes.

As a final verification of these results, it is worth asking how well our analytic results, which only consider edge diffraction effects, line up with the exact Fast Fourier

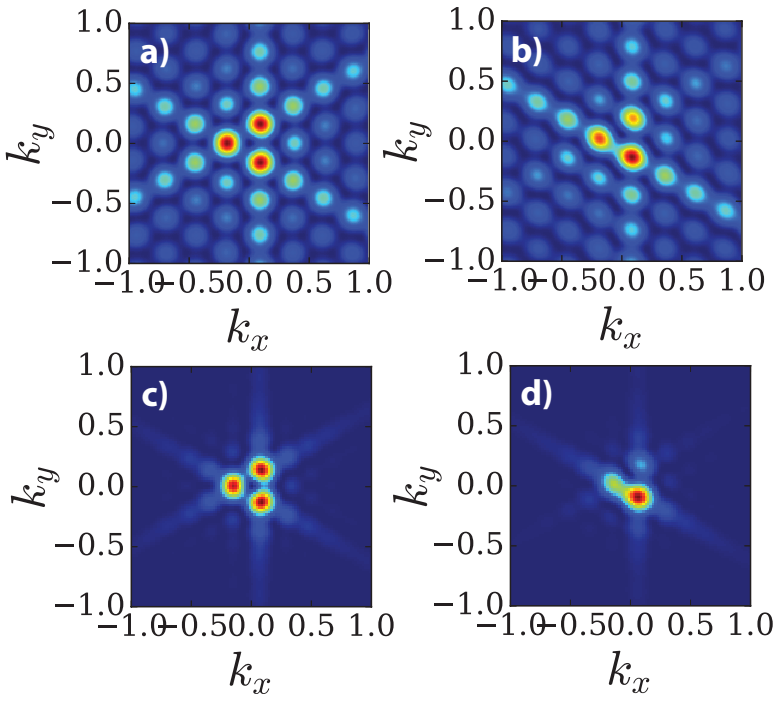

Figure 4.8: Comparison of the analytic result with the FFT result, for $m = 1$, $y_0 = 0$ and (a), (c) $x_0 = 0$ FFT and analytic, (b), (d) $x_0 = 0.159a$, FFT and analytic.

Transform (FFT) calculation of the diffracted field from the full aperture. An example of this comparison is shown in Fig.4.8, for horizontal displacement of the vortex center. The primary multispot intensity structure is the same for both methods, but there is a large array of secondary spots visible in the analytic result that are not present in the exact result. Additionally, the central lobed pattern seems to be lost more quickly upon displacement in the exact result. However, these results show that the analytic calculation maintains the most important aspects of the diffraction patterns.

4.3 Exact Analytical Solution

In the previous sections, we have emphasized that our analytical model is useful both for understanding the underlying physics and for providing qualitatively accurate results for diffraction through a triangular aperture. It is worth noting here, however, that it is possible to extend the edge diffraction integral to an integral over the entire area of the triangle and that this too may be evaluated analytically. This was not done for the bulk of this chapter because the result is significantly more complicated and does not provide the same physical insight as the simpler model, thus trading precision for clarity. Furthermore, the process outlined introduces a removable singularity at $\kappa = 0$ in the solution, which must be accounted for. We include the calculation here for the sake of completeness.

We integrate Eq. (4.18) over the side length a from 0 to A, where now we use A is the edge length of the triangular aperture. This integral must be multiplied by $\sqrt{3}/6$ in order for the total integral over l and a to cover an area equal to one-third of the total triangle area.

It is to be noted that the derivative of Eq. (4.18) could be pulled completely outside the integrand if not for the presence of the second exponential from the left. To deal with this, we let $\kappa \to \kappa'$ in the exponent and then take the limit in the end as $\kappa' \to \kappa$, or

$$U(k_x, k_y) \sim \frac{\sqrt{3}}{6}(i\alpha)^m |\alpha| \frac{\partial^m}{\partial \kappa^m} \left\{ e^{-i\chi a} e^{i(\kappa'-\kappa)(a\beta - z_0)/\alpha} \frac{\kappa a/2}{\kappa/2} \right\}_{\kappa'=\kappa}. \tag{4.22}$$

Writing the sine function as complex exponentials, we have the expression

$$U(k_x, k_y) \sim 2\frac{\sqrt{3}}{6}(i\alpha)^m |\alpha| \frac{\partial^m}{\partial \kappa^m} \left\{ e^{-i(\kappa'-\kappa)z_0/\alpha} \frac{e^{-i\chi a}}{\kappa} \times e^{i(\kappa'-\kappa)a\beta/\alpha} \frac{e^{i\kappa a/2} - e^{-i\kappa a/2}}{2i} \right\}_{\kappa'=\kappa}. \tag{4.23}$$

Now the variable a only appears in complex exponents. We may readily integrate with respect to a to find

$$U(k_x, k_y) \sim a\frac{\sqrt{3}}{6}(i\alpha)^m|\alpha|\frac{\partial^m}{\partial\kappa^m}\Bigg\{\frac{e^{-i(\kappa'-\kappa)z_0/\alpha}}{i\kappa} \times [e^{i\delta_+}j_0(\delta_+) - e^{i\delta_-}j_0(\delta_-)]\Bigg\}_{\kappa'=\kappa}, \tag{4.24}$$

where

$$j_0(x) = \frac{\sin(x)}{x} \tag{4.25}$$

is the zeroth order Bessel function and for brevity we have introduced

$$\delta_\pm \equiv a[-\chi + (\kappa' - \kappa)\beta/\alpha \pm \kappa/2]/2. \tag{4.26}$$

Each side of the triangle may be treated in the same manner to derive the total field. For small values of m, the derivatives may be calculated analytically and the limit taken to get the final result. A comparison between the exact FFT result and the results derived from Eq.(4.24) is shown in Fig.(4.9), and it can be seen that there is an excellent correspondence in numeric and analytic results.

4.4 Conclusion

We have derived an analytic model for the diffraction of a vortex beam by a triangular aperture and have used this model to provide insight into the nature of the diffraction pattern that arises. The model also allows us to estimate the stability of the vortex diffraction pattern in a number of circumstances, including off-axis beams and mixed-mode beams. Though the system appears to be relatively stable with respect to off-axis detection of a vortex, it does not appear to be as suitable for mixed mode beams, as the higher order modes are generally overwhelmed by the lower-order

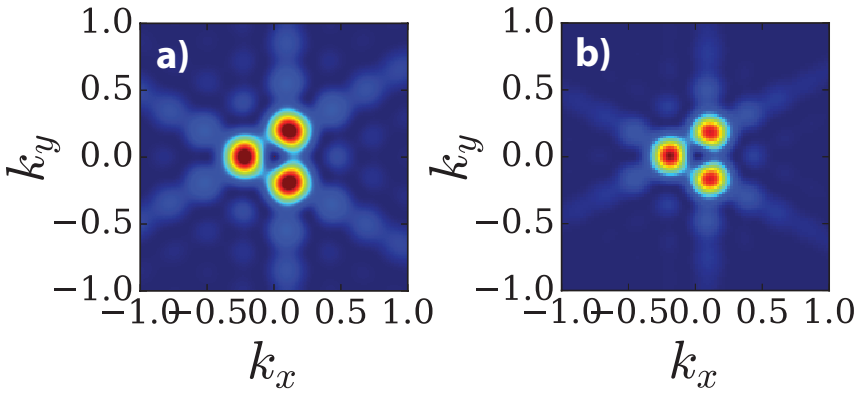

Figure 4.9: Comparison of the diffraction pattern of an $m = 1$ vortex from (a) the FFT calculation and (b) the analytic formula, Eq.(4.24).

modes in the diffraction pattern. The results are in good agreement with exact FFT calculations.

CHAPTER 5: PROPAGATION OF VORTEX BEAMS THROUGH THE ATMOSPHERE

It has been mentioned several times already that one of the potential uses for partially coherent vortex beams (PCVBs) is in free-space communication. Some work has been done showing coherent vortex beams doing well in free-space communication experiments [61, 62, 63]. Partially coherent beams are less prone to speckle and vortex cores are more stable under turbulence than non-vortex beams. Therefore a combination may be advantageous in applications that require clean propagation over large distances in a non-uniform medium. In this chapter we present the results of simulation work on the propagation of PCVBs through turbulent atmosphere.

5.1 Methodology Background

One of the major difficulties in studying free-space propagation of beams is the complex nature of the atmosphere. Temperature, time of day, wind, humidity, pollution and other variables [64, Chapter6] all affect the optical profile. The atmosphere is not static but turbulent, leading to continuous random fluctuations in the optical properties of a beam's path. Developing a model that describes these effects in all circumstances while remaining tractable has proved a challenge. A rigorous and general theory for atmospheric propagation is still awaiting development, although researchers have well-developed models for certain asymptotic regimes, particularly weak fluctuations [65].

The Rytov approximation remains a useful tool for studying the propagation of waves under weak fluctuations. While it can be used to directly calculate the mean propagated field for short distances, it codifies into several coefficients the physical

parameters that can be used to describe the overall effect of propagation through random media. In particular, it gives us the index of refraction structure parameter of the atmosphere, $C_n^2(\ \mathrm{m}^{-2/3})$, and the *Rytov variance*, σ_1^2, which is rigorously speaking the scintillation index of an unbounded plane wave in weak fluctuations, and roughly speaking is a measure of the influence of turbulence on an optical beam. When using this parameter, we can characterize conditions where $\sigma_1^2 < 1$ as weak turbulence conditions, and moderate to strong turbulence as $\sigma_1^2 \geq 1$.

It also incorporates the concept of the power spectrum to describe the spatial correlations of the refractive index. A number of power spectra have been proposed, but all have limitations. The Kolmogorov spectrum is the simplest,

$$\Phi_n(\boldsymbol{\kappa}) = 0.033 C_n^2 \boldsymbol{\kappa}^{-11/3}, \tag{5.1}$$

but is limited in validity to the range

$$2\pi/L_0 < \boldsymbol{\kappa} < 2\pi/l_0, \tag{5.2}$$

where $\boldsymbol{\kappa}$ is the wavenumber, l_0 is the inner scale, which describes the smallest eddy size, and L_0 is the outer scale, which describes the largest eddy size [64][2.2]. Larger eddies exhibit a laminar type flow, while smaller eddies are dissipative. Thus the Kolmogorov power spectrum is limited to the so-called *inertial range*, as is the von Kármán spectrum[64, Section 2.2],

$$\Phi_n(\boldsymbol{\kappa}) = 0.033 C_n^2 (\boldsymbol{\kappa}^2 + \boldsymbol{\kappa}_0^2)^{-11/6}, \tag{5.3}$$

which is valid when

$$0 < \boldsymbol{\kappa} < 2\pi/l_0. \tag{5.4}$$

If effects outside this range must be accounted for, other spectrums must be employed. We will be restricting ourselves to the weak turbulence, inertial range, and be using the Kolmogorov power spectrum.

Unfortunately, while the Rytov method gives us useful tools for characterizing the atmosphere, it is not well suited to analyzing longer propagation distances. In theory, one could use the extended Huygens-Fresnel principle [65, Section 1.4.2], which describes the optical wave field at the detector as

$$U(\mathbf{r}, L) = -\frac{ik}{2\pi L} \exp[ikl] \int \int_{-\infty}^{infty} U_0(\boldsymbol{s}, 0) \exp\left[\frac{ik|\boldsymbol{s} - \mathbf{r}|^2}{2L} + \psi(\mathbf{r}, \boldsymbol{s})\right], \tag{5.5}$$

where the point $(\boldsymbol{s}, 0)$ is the origin of a spherical wave propagating to point $(\mathbf{r}, L)$ and $\psi(\mathbf{r}, \boldsymbol{s}) = \psi_1(\mathbf{r}, \boldsymbol{s}) + \psi_2(\mathbf{r}, \boldsymbol{s})$ is the random component of the complex phase of the wave, to study longer distance propagations. However, employing the extended Huygens-Fresnel principle to analytically propagate a beam is prohibitively complex for all but a few special cases, such as Gaussian, spherical or planar waves. The primary equation of interest when employing the extended Huygens-Fresnel principle is a fourth order moment generating function that involves eight integrals, and relies on the ensemble average of three other second order moment generating functions (see [65][1.4.2]). Simpler models may give reasonable approximations in small ranges, but fail to account for all observed effects. Direct simulation may seem a possibility in an age of cheap processing, but the large number of variables makes this extremely time costly. One modeling method that strikes an effective balance between these concerns is the thin phase screen propagation method introduced by Knepp [66] and discussed by Martin and Flatté [67]. This method treats the atmosphere's optical profile not as a continuous, fluctuating medium but as a series of static, randomly generated phase screens of infinitesimal thickness and simulates propagation via a series of Discrete Fourier Transforms (DFT). A 256×256 array is typically sufficient,

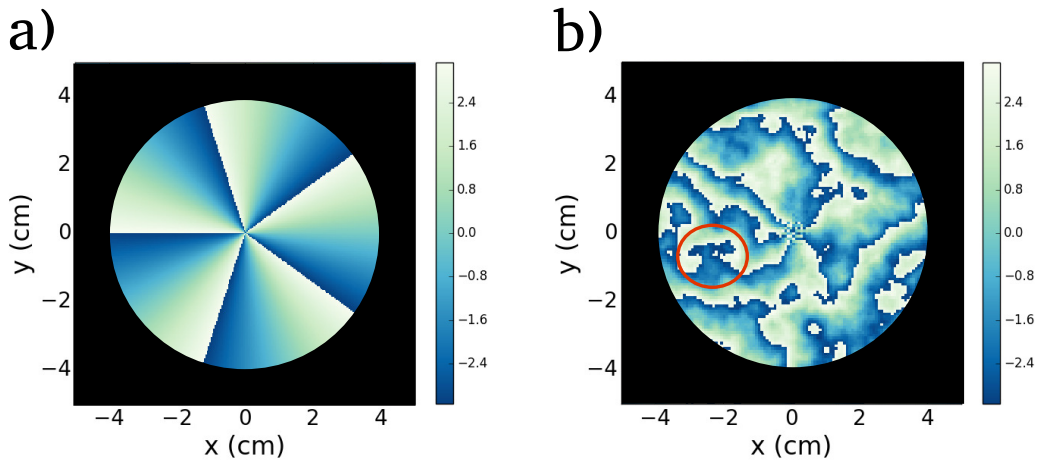

Figure 5.1: Sample plot of the phase structure of a coherent vortex beam in the a) source plane b) detector plane after 10 km of propagation through turbulence with a Rytov variable of $\sigma_1^2 = .954$. The black mask is present to show only what would be seen by a detector. The red circle highlights the creation of a vortex pair.

with an appropriate number of iterations, to model the essential behavior of a beam through weak to moderate turbulence. The basic procedure for a single phase screen interaction/propagation for a beam $\psi(\mathbf{r})$ with a phase screen $\Phi(\mathbf{r})$, traveling in the z-direction, is

1. $\psi(\mathbf{r}, z) = \psi(\mathbf{r}, z_-) \exp[i\Phi(\mathbf{r})]$
2. DFT $\psi(\mathbf{r}, z) \rightarrow \Psi(\boldsymbol{\kappa}, z)$
3. $\Psi(\boldsymbol{\kappa}, z'_-) = \Psi(\boldsymbol{\kappa}, z) \exp[-i\boldsymbol{\kappa}^2 \Delta z / 2k]$
4. Inverse DFT $\Psi(\boldsymbol{\kappa}, z'_-) \rightarrow \psi(\mathbf{r}, z'_-)$.

It is worthwhile to go into each of these steps in more detail, as there is some subtlety in both the implementation and in the notation. In the first step, the field impinging on the screen is "scrambled" by the randomly generated phase screen, which for every element in the array involves a small, random phase perturbation. The new scrambled field then undergoes a discrete Fourier Transform into κ-space, where it is then "propagated" for the inter-screen distance, Δz. The bounds of κ-space will depend on the programmer's choice of κ, generally either a von Kármán or

a Kolmorgorov type. We chose a Kolmorgorov spectrum with cutoff. This scrambled, propagated field is then inverse Fourier Transformed back into ρ-space, and represents the field about to impinge on the next phase screen. An example of this process, implemented in Python using the Numpy package, is

```
def Propagate(beamArray, screenArray, deltaz, k, kappaArray):
"""
Models the propagation through a single screen array.
"""
temp1 =  beamArray*exp(I*screenArray)
temp2 = fftshift(fft2(temp1))
temp3 = temp2*exp(-I*kappaArray**2 *deltaz/(2*k))
newfield = ifft2(fftshift(temp3))
return newfield
```

This algorithm can then be incorporated into a function to model the propagation over multiple screens to simulate propagation over a long distance and changes in atmosphere. The thin phase screen method is relatively straightforward to implement in the coding environment of the researcher's choice, and is flexible enough to study a wide variety of beams and conditions[1]. For example, it was employed by Cheng *et alia* to study the propagation of vector vortex beams and compare them to scalar vortex beams and fundamental Gaussians[69]. An example of the phase structure of a coherent vortex beam, $m = 5$, after such simulated propagation is shown in Figure 5.1. While the 5 increases from 0 to 2π can still be seen the beam is visibly scrambled.

5.2 Beam Comparisons

There are a number of different beam arrangements that are potentially better information carriers through turbulence than a coherent vortex beam. In this section we explore four such beams and compare each to a standard coherent vortex beam. In

[1] including acoustic waves instead of optical ones [68].

each case, the wavenumber $k = 40536$ cm^{-1}, the beam (or beamlet) waist $w_0 = 2$ cm, and the detector radius is 4 cm.

While the topological charge of a beam is a conserved quantity, there are two factors which can result in its "loss" at the detector, which is only able to detect the net topological charge around its edge. The first is that turbulence can induce pair formation, whereby a pair of vortices of opposite sign are spontaneously formed. Since they have opposite charge, the total charge of the beam is conserved, but if one of these pairs is near the edge of the detector, or only one is within the detector and the other lies entirely outside, this can alter the detected topological charge of the beam. The second is the fact that turbulence can alter the path of the vortex core or cores enough to push them out of the detectors boundaries. Small changes in inclination, over the course of several kilometers, can easily result in a vortex core missing a detector whose radius is only on the order of centimeters. A beam which is more prone to wander out of the detector will therefore have greater variability in the detected charge, which would pose a problem in certain applications, such as multiplexing data through beams of different charge.

5.2.1 Coherent Vortex Array

One beam configuration that may improve the distance at which a topological charge is detectable through turbulence is a coherent array of beams (CAB). The thought behind this configuration is that while a single-vortex, high-order coherent beam (SVCB) may wander outside the detector range, losing completely the ability to be detected, multiple first-order vortices may wander independently and increase the chance that at least some charge remains detectable. Such a beam with m singularities in this case would be described as

$$U(x,y) = [(x - x_1) + i(y - y_1)][...][(x - x_m) + i(y - y_m)] \exp[-(x^2 + y^2)/w0^2], \tag{5.6}$$

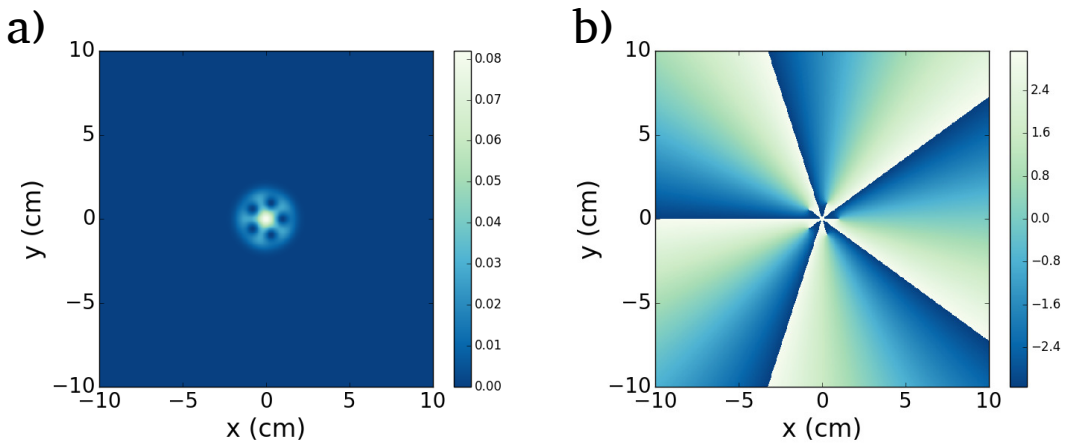

Figure 5.2: Sample plots of the a) intensity and b) phase of a coherent radial array in the source plane.

with

$$x_j = R\cos(2\pi j/m), \tag{5.7}$$

$$y_j = R\sin(2\pi j/m), \tag{5.8}$$

which produces a beam in the source place with charge m. The intensity and phase of such a beam are shown in Fig 5.2. It has a bright central core with the singularities arrayed around the edge of the beam. The phases of the beamlets combine to form an m order phase. However, as can be seen in Fig 5.3, after passing through turbulence the beams quickly degrade as the single charge beams rapidly wander outside the detector radius. After the 10 km propagation, the SVCB still has a detectable charge of $t = 4.539 \pm 0.588$, while the CAB has a charge of $t = 0.9575 \pm 0.728$. This holds true regardless of how tightly the CAB is formed, as can be seen in Fig 5.3. The CAB in Fig 5.3a has its component vortices arranged only 0.1 mm apart, but its propagation is not improved over the CAB where the vortices are arranged 1.0 cm apart, as seen in Fig 5.3b. Regardless of the configuration, the CAB is highly susceptible to turbulence and is only poorly detected.

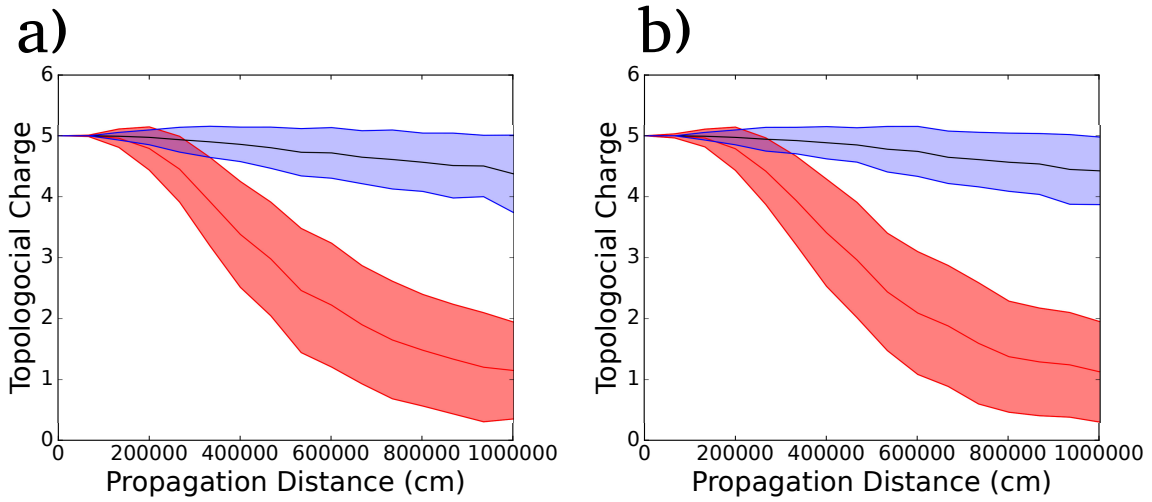

Figure 5.3: Coherent Array Beam compared with a coherent beam on propagation. The blue shading shows the standard deviation away from the average detected topological charge of the coherent beam, while the red shading shows the same for the coherent array beam. The radius at which the beamlets are placed is a) $r = .01$ cm and b) $r = 1.0$ cm. Propagated 10 km with a Rytov variance of 0.95 using 10 phase screens.

5.2.2 Incoherent Vortex Radial Array

If a coherent array of beams fails to propagate well, it is not unreasonable to ask how an incoherent array of beams (ICAB) propagates. That is, instead of generating a beam in the manner of Eq. (5.6), we compose an array of "beamlets"

$$u(x, y) = ((x - x_j) + i(y - y_j))^m \exp[-(x^2 + y^2)/w0^2], \tag{5.9}$$

with x_j, y_j as defined in Eq. (5.7) for N beamlets. The beamlets are taken to be incoherent, i.e. they do not interfere with each other. Note that unlike the coherent array, each beamlet must have charge m for the overall beam to have charge m. A set of randomized phase screens is generated, and each beamlet is simulated propagating through separately, and the topological charge found for its individual propagation. The total topological charge is the unweighted sum of the individual topological charges. Once all N beamlets have been propagated through the same set

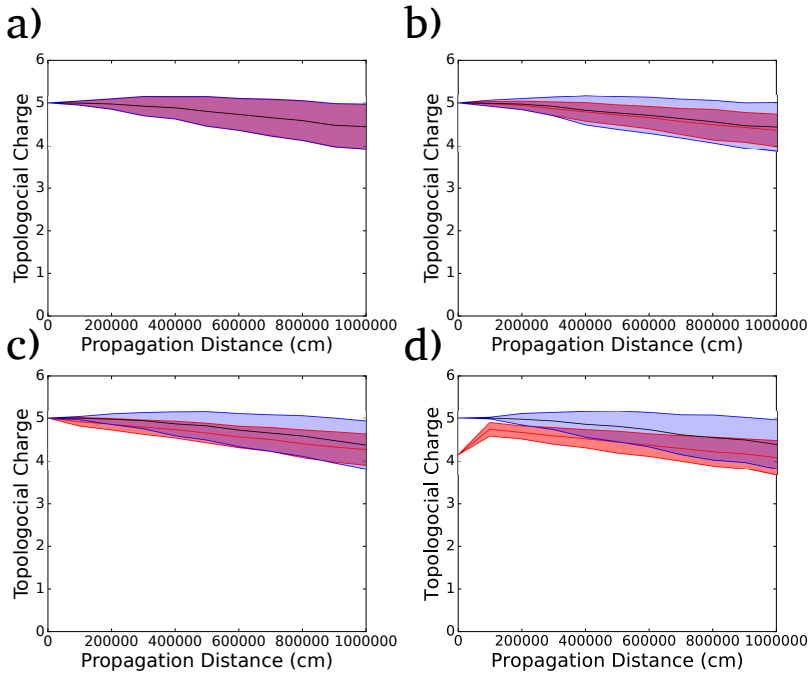

Figure 5.4: Plots showing the detectable topological charge as a function of propagation distance for a ICAB, for arrays of different radii: a) $r = 0.01$ cm b)$r = 0.1$ cm c) $r = 1.0$ cm d) $r = 2.0$ cm. The blue shading shows the standard deviation away from the average detected topological charge of the coherent beam, while the red shading shows the same for the incoherent array beam. Propagated 10 km with a Rytov variance of 0.95 using 10 phase screens.

of screens, a new set of screens are generated and the process repeated for the chosen number of iterations. Propagated in this manner, the beamlets cannot interfere with each other.

As can be seen in Figure 5.4, the ICAB does significantly better than the CAB (Fig. 5.3). For $N = 5$, however, it only has slight advantages over a SVCB. For a tightly arranged array, there is no advantage over a SVCB, but at a wider spacing, roughly 50-75% of the beam width w_0, the ICAB experiences less variance in its detected topological charge. A rather odd feature is observed when the radius of the array is the same as the beam width (Fig. 5.4d). In the source plane there is a large drop in detected topological charge that after propagation increases for a short distance.

With this range of radial array values, we can examine whether the number of beamlets has an effect on the array's detectable charge. As seen in Figure 5.5, a larger

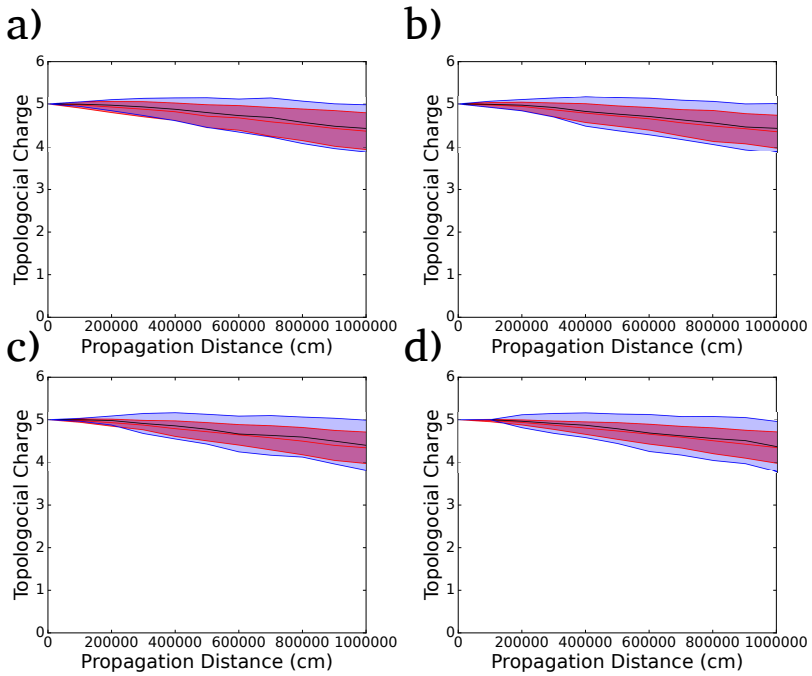

Figure 5.5: Comparison of ICABs with different numbers of beamlets. a) $N = 3$ b) $N = 5$ c)$N = 10$ d)$N = 20$. The blue shading shows the standard deviation away from the average detected topological charge of the coherent beam, while the red shading shows the same for the incoherent array beam. Propagated 10 km with a Rytov variance of 0.95 using 10 phase screens.

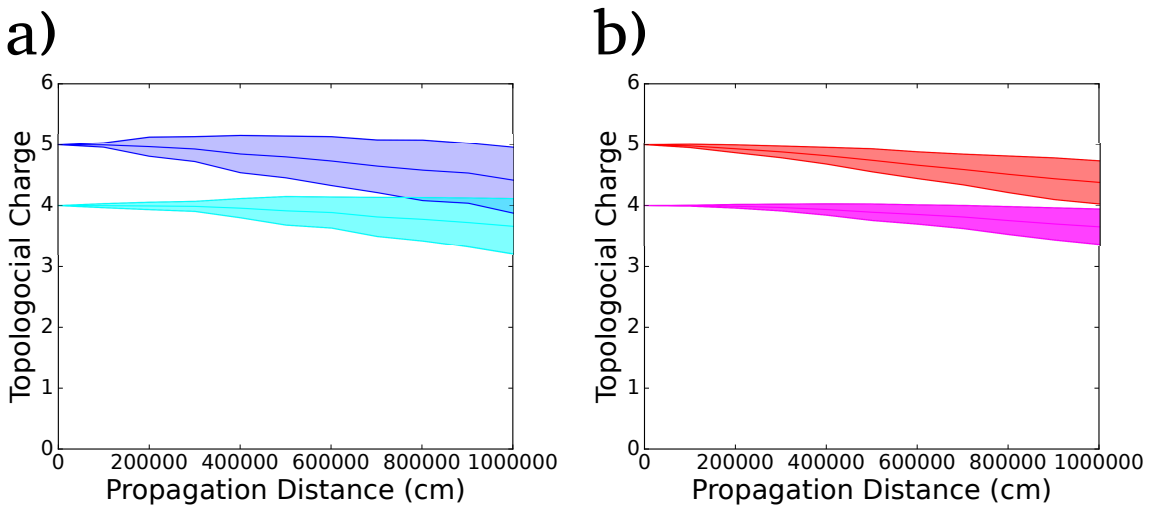

Figure 5.6: Comparison of a) two SVCB, $m = 5$ and $m = 4$ and b) two $N = 20$ ICAB, $m = 5$, $m = 4$. The shaded areas represent the varience in the detected charge. While the varience in the SVCBs overlaps, leading to uncertainty in which beam is detected, the smaller varience in the ICAB eliminates this uncertainty.

number of beamlets results in a reduction in charge variance, but does not improve the average topological charge detected over a coherent beam. The reduction in the variance of the detected charge may be desirable, such as to avoid overlap between the detected charge of higher and lower order ICABs in multiplexed beams.

5.2.3 Ponomerenko Partially Coherent Beams

Another type of partially coherent beam composed of mixed modes, described by Ponomerenko *et alia* in [32]. This beam class is defined by its cross-spectral density being of the form

$$W(x,y) = \sum_{n=0}^{m} \lambda_{nm} u^*_{nm}(x,y) u_{nm}(x',y') \tag{5.10}$$

where each mode is

$$u_{nm} = \left(\frac{(x \pm iy)}{w(z)}\right)^{|m|} L_n^{|m|}\left(\frac{2(x^2+y^2)}{w_0^2}\right) \exp\left[\frac{-(x^2+y^2)}{w_0^2}\right] \tag{5.11}$$

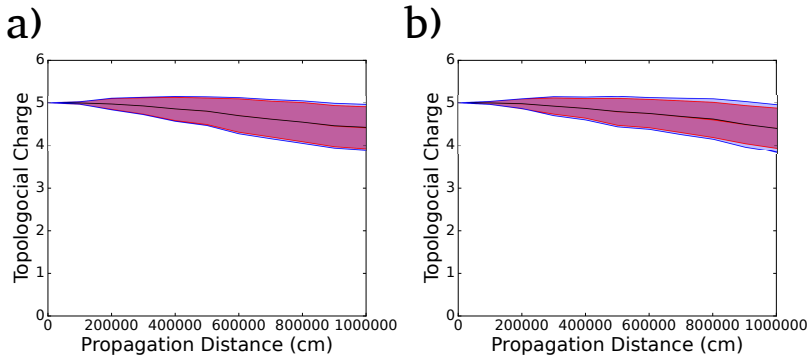

Figure 5.7: PMM beam with $n_{max} = 5$, $m = 5$ with a) $\lambda_{nm} = 0.1$ and b) $\lambda_{nm} = 1.0$. Propagated 10 km with a Rytov variance of 0.95 using 10 phase screens.

and λ_{nm} provides the modal weights. This is simulated in a similar manner to the partially coherent radial array. Each mode is separately propagated through a set of phase screens, the topological charge calculated for each mode, and saved in an array. After each mode has been propagated through the full set of screens, the total detected topological charge is calculated as a weighted sum of the modal charges. A new set of screens is generated, and the process is repeated for enough iterations to result in a stable average.

As seen in Figure 5.7, a more incoherent beam shows a very small reduction in detected topological charge spread. However, λ_{nm} is not the only parameter that may be varied. We may also inquire into the effect of larger or smaller n_{max} on the detectable charge. Since λ_{nm} equal to unity gives the most reduction in spread, we use that value for all λ_{nm} in our comparison. As seen in Figure 5.8, a larger n_{max} leads to a greatly reduced detected topological charge spread on propagation, and a slight reduction in the rate at which the detected charge drops, but at a cost to overall detected charge. For every additional 10 orders to n_max, there is a drop of $\sim .25$ in the detected charge, beginning in the source plane. For an $n_max = 20$ for an $m = 5$ beam, the detectable charge in the source plane is ≈ 4.5, and for $n_max = 30$ for an $m = 5$ beam, the detectable charge in the source plane is only ≈ 4.25. Thus for this beam class, stability and low variance comes at the cost of overall detectable

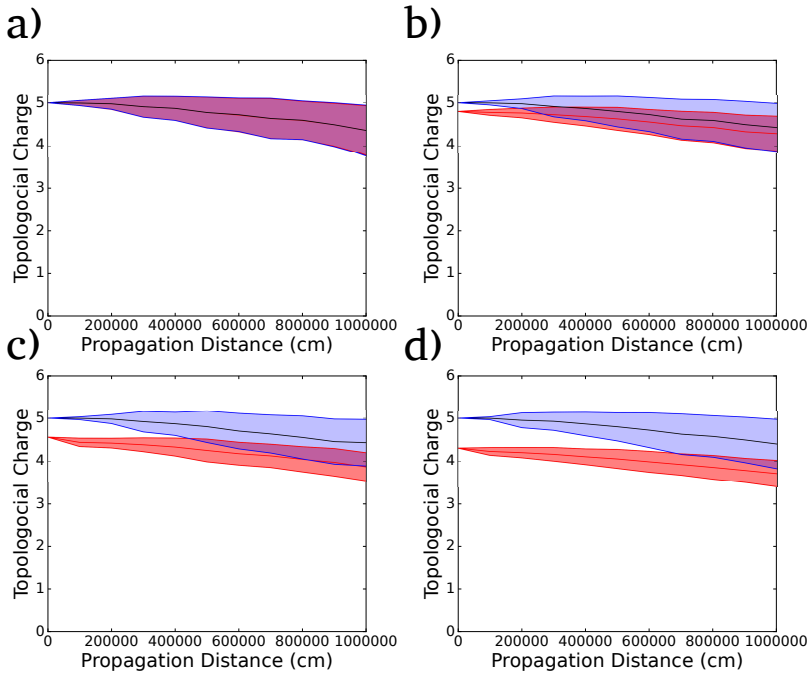

Figure 5.8: PMM beam comparison with $\lambda_{nm} = 1.0$ and a) $n_{max} = 2$, b) $n_{max} = 10$, c) $n_{max} = 20$, and d) $n_{max} = 30$. Propagated 10 km with a Rytov variance of 0.95 using 10 phase screens.

charge for the entire propagation.

5.2.4 Beam Wander Model Partially Coherent Beams

Finally, we look at a partially coherent beam class which approximates by the beam wander model used in Chapter 3. This beam class combines elements of the incoherent radial array and the Ponomerenko beams. The beams are composite beams; like the Ponomerenko beams each beamlet is individually weighted, and like the incoherent array the vortex cores are not placed in the center of the beam. In this case, the beamlets are given a random position and the beamlets given a weight based on their position and the selected coherence parameter δ, so that

$$u(x, y, \delta) = ((x - \delta_{nx}) + i(y - \delta_{ny}))^m \exp\left[\frac{-(x^2 + y^2)}{w_0^2}\right] \tag{5.12}$$

where δ_{nx}, δ_{ny} are randomly generated numbers from a normal distribution of width δ. Each beamlet's weight, Δ_n is calculated by

$$\Delta_n = \exp\left[\frac{-(\delta_{nx}^2 + \delta_{ny}^2)}{\delta^2}\right] \tag{5.13}$$

for each of N beamlets. We will refer to this model for brevity as the beam wander vortex beam (BWVB). As with the two previous beam classes, each beamlet is propagated by itself through a set of randomized phase screens and its topological charge determined. This is repeated for each of the N beamlets, and a weighted sum is taken as the total detected topological charge.

This gives several parameters to vary for each beam. The number of beamlets is an obvious place to begin. As seen in Figure 5.9, there is an advantage both in terms of average detected charge and the variance to using a larger number of beams. A beam composed of $N = 5$ beamlets has a variance of $\Delta t = \pm.49$, while a beam with $N = 25$ has $\Delta t = \pm.32$. However, increasing the number of beamlets indefinitely does not increase performance. A beam with $N = 50$ has $\Delta t = \pm.31$, which is not very different from an $N = 25$ beam, but with $\sim 30\%$ greater computational time.

If instead we hold the number of beams constant but vary δ, we can see the effect of the coherence parameter on the propagation. As seen in Figure 5.10, for a small δ the beam approaches the coherent case, as expected. For a larger coherence parameter of $\delta = 1.0$ cm the variance is reduced compared to the coherent case, but there is no difference in the average topological charge after propagation. For a large coherence parameter of $\delta = 2.0$ cm, the detectable charge is reduced, albeit slightly, in the source plane, with a significant topological charge variance even in the source plane and the detectable charge continues to drop over the course of the propagation more steeply than the coherent beam. However, the variance at the detector plane is roughly half that of the coherent plane.

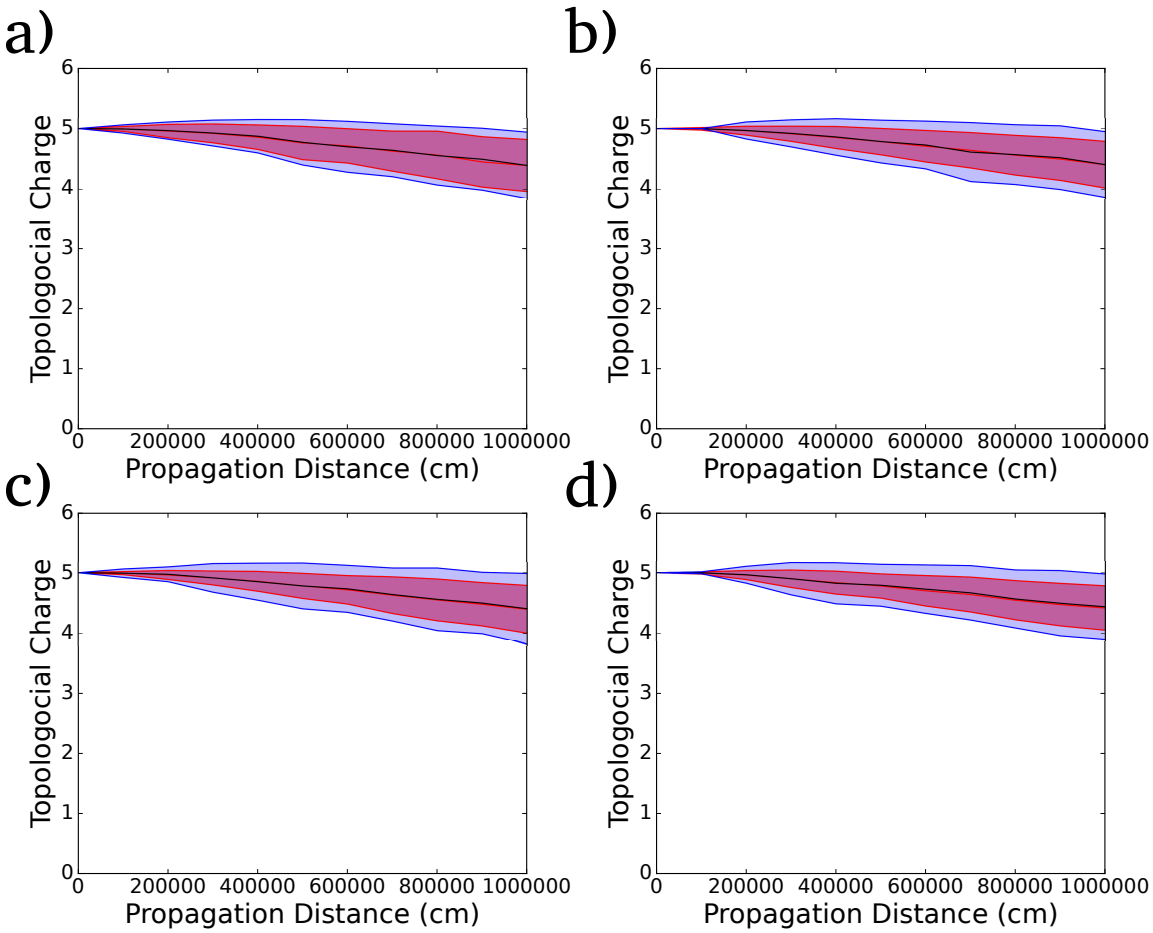

Figure 5.9: BWVB with $\delta = 0.5$ and numbers of beamlets a) $N = 5$, b) $N = 25$, c) $N = 50$, and d) $N = 100$. Propagated 10 km with a Rytov variance of 0.95 using 10 phase screens.

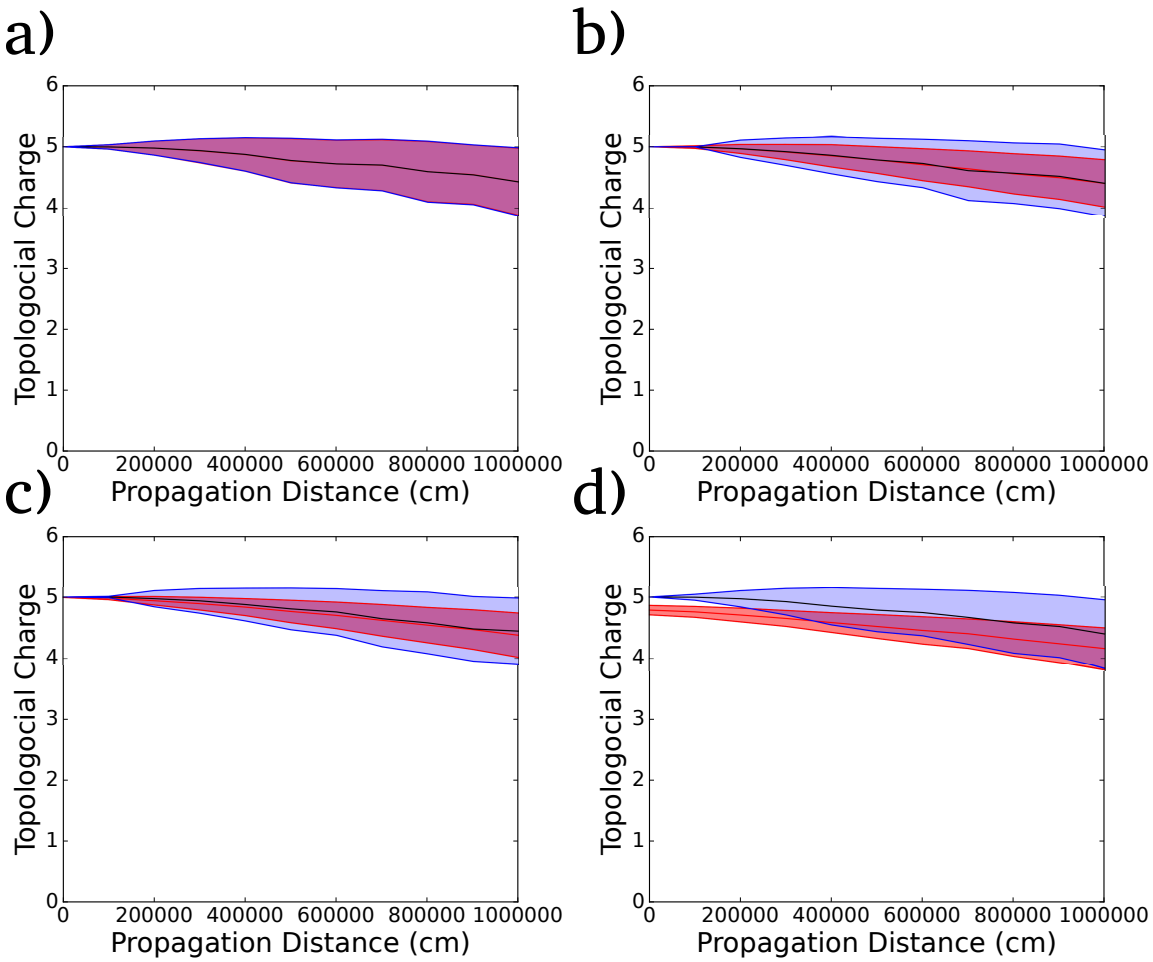

Figure 5.10: Comparison of BWVB with $N = 25$ and a) $\delta = 0.1$ cm, b) $\delta = 0.5$ cm, c) $\delta = 1.0$ cm, and d) $\delta = 2.0$ cm. Propagated 10 km with a Rytov variance of 0.95 using 10 phase screens.

5.3 Conclusions

A few broad conclusions may be drawn from the variety of beam propagations presented above. Compared to coherent beams with a single vortex core, coherent beams with the vortex cores split propagate very poorly except over very short distances. Partially coherent beams exhibit less variance as the beams propagate, but do not improve overall charge detectability. Incoherent arrays of vortex beams propagate significantly better than coherent beams, and beams of different initial charge values remain distinct after 10 km of propagation.

CHAPTER 6: CONCLUSIONS

In this thesis, we have set forth to advance the study of correlation vortices by providing a complete description of a partially coherent beam class, to provide a theoretical foundation for a promising vortex charge detection method, and examine the propagation characteristics of a number of incoherent, partially coherent and fully coherent beams for their potential use in free space communication. This work was undertaken to increase our understanding of different types of optical and correlation vortex beams, in the hopes that with increased understanding and theoretical foundation other researchers may utilize these beams in fields as diverse as astronomy and biology.

In Chapter 3, we first derived a complete description of a partially coherent Laguerre-Gauss beam of the first azimuthal order, both in the source plane and on propagation. We showed that the correlation vortices will only occur in transverse planes, i.e. $z_1 = z_2 = z$, and that the correlation vortices undergo a non-trivial twist on propagation. We then went on to describe an infinite class of partially coherent vortex beams, derived using azimuthal Laguerre-Gauss beams and the beam wander model for construction of partially coherent beams. From this we were able to demonstrate some limitations of the beam wander model, namely that beams constructed in this manner will have a coherence length limited by the width of the beams, and that the coefficients of the beam have a Gaussian-Schell structure. We were also able to describe the orbital angular momentum of the beam by deriving the orbital angular momentum flux density, roughly understood as the angular momentum per photon, and showed that it has the structure of a Rankine vortex for highly and moderately coherent beams. Further work could be done by examining PCVBs constructed of LG

beam of any radial or azimuthal order, or constructed beams with the beam wander model and other types of coherent vortex beams.

In Chapter 4, we undertook to give a rigorous theoretical foundation to the well known phenomena of vortex diffraction through a triangular aperture. We first laid out a derivation using both amplitude and phase of the beam but taking into account only the edge diffraction effects, in accordance with established principles of geometrical optics, and demonstrated that this model gives considerable insight into the origin of the lobe patterns. For completeness and comparison's sake we then calculated the diffraction over the entire aperture. We showed that the edge-diffraction case gave much the same results as the more rigorous exact calculation, but with addition insight and tractability. We showed that this model, unlike previous work, was able to model diffraction for beams imperfectly aligned with the aperture, and mixed mode beams, although the method is more suited to the former than the latter. Finally, we compared results from our calculations to that of exact Fast Fourier Transform, and found them to be in good agreement. Further work would investigate its possibilities for detecting the charge of partially coherent beams, using pattern recognition algorithms to adjust the alignment of the beam, and any advantages apertures with more sides might have.

Finally in Chapter 5, we examined how well incoherent, partially coherent and fully coherent vortex beams propagate through 10 km of atmospheric turbulence. We employed the thin phase screen method of simulating the propagation of waves through turbulence and found that while partially coherent beams experienced less variance on propagation than a coherent vortex beam, a coherent vortex array fails to propagate except over very short distances. Incoherent arrays propagated with the least amount of variance and different orders remain distinguishable after 10 km of propagation. This characteristic may be useful in applications such as free-space communication, and data multiplexing.

REFERENCES

[1] A. A. Michelson and E. W. Morley, "On the relative motion of the earth and of the luminiferous ether," *Sidereal Messenger, vol. 6, pp. 306-310*, vol. 6, pp. 306–310, 1887.

[2] T. Young, "The bakerian lecture: Experiments and calculations relative to physical optics," *Philosophical transactions of the Royal Society of London*, vol. 94, pp. 1–16, 1804.

[3] R. Staley, *Einstein's Generation: The Origins of the Relativity Revolution*. University of Chicago Press, 2008.

[4] E. Verdet, "Étude sur la constitution de la lumiere non polarisée et de la lumiere partiellement polarisée," in *Annales Scientifiques de l'Ecole Normale Supérieure*, vol. 2, pp. 291–316, Elsevier, 1865.

[5] A. A. Michelson, "I. on the application of interference methods to astronomical measurements," *The London, Edinburgh, and Dublin Philosophical Magazine and Journal of Science*, vol. 30, no. 182, pp. 1–21, 1890.

[6] A. A. Michelson, "Xxviii. visibility of interference-fringes in the focus of a telescope," *The London, Edinburgh, and Dublin Philosophical Magazine and Journal of Science*, vol. 31, no. 190, pp. 256–259, 1891.

[7] A. A. Michelson, "Xxx. on the application of interference methods to spectroscopic measurements. ii," *The London, Edinburgh, and Dublin Philosophical Magazine and Journal of Science*, vol. 34, no. 208, pp. 280–299, 1892.

[8] M. Born and E. Wolf, "Principles of optics, 7th (expanded) ed," *Cambridge U. Press, Cambridge, UK*, p. 890, 1999.

[9] M. Von Laue, "Die entropie von partiell koharenten strahlenbundein," *Annalen der Physik*, vol. 23, pp. 1–43, 1907.

[10] M. Berek, "Über kohärenz und konsonanz des lichtes," *Zeitschrift für Physik A Hadrons and Nuclei*, vol. 36, no. 9, pp. 675–688, 1926.

[11] M. Berek, "Das problem der quantitativen mikroskopie der erzmineralien und seine lösung," *Zeitschrift für Kristallographie-Crystalline Materials*, vol. 76, no. 1-6, pp. 396–430, 1931.

[12] P. H. van CITTERT, "Die wahrscheinliche schwingungsverteilung in einer von einer lichtquelle direkt oder mittels einer linse beleuchteten ebene," *Physica*, vol. 1, no. 1-6, pp. 201–210, 1934.

[13] P. Van Cittert, "Kohaerenz-probleme," *Physica*, vol. 6, no. 7-12, pp. 1129–1138, 1939.

[14] E. Wolf, "A macroscopic theory of interference and diffraction of light from finite sources. ii. fields with a spectral range of arbitrary width," in *Proceedings of the Royal Society of London A: Mathematical, Physical and Engineering Sciences*, vol. 230, pp. 246–265, The Royal Society, 1955.

[15] A. Blanc-Lapierre and P. Dumontet, "La notion de cohérence en optique," *Revue d'Optique Théorique et Instrumentale*, vol. 34, no. 1, pp. 1–21, 1955.

[16] E. Wolf, *Introduction to the Theory of Coherence and Polarization of Light*. Cambridge University Press, 2007.

[17] M. V. Berry, "Geometry of phase and polarization singularities, illustrated by edge diffraction and the tides," in *Proc. SPIE*, vol. 4403, 2001.

[18] A. Sommerfeld, "Optics: Volume iv of lectures on theoretical physics..," 1964.

[19] J. Nye and M. Berry, "Dislocations in wave trains," in *Proceedings of the Royal Society of London A: Mathematical, Physical and Engineering Sciences*, vol. 336, pp. 165–190, The Royal Society, 1974.

[20] J. F. Nye, *Natural focusing and fine structure of light: caustics and wave dislocations*. CRC Press, 1999.

[21] J. Nye, J. Hajnal, and J. Hannay, "Phase saddles and dislocations in two-dimensional waves such as the tides," in *Proceedings of the Royal Society of London A: Mathematical, Physical and Engineering Sciences*, vol. 417, pp. 7–20, The Royal Society, 1988.

[22] J. Poynting, "The wave motion of a revolving shaft, and a suggestion as to the angular momentum in a beam of circularly polarised light," *Proceedings of the Royal Society of London. Series A, Containing Papers of a Mathematical and Physical Character*, vol. 82, no. 557, pp. 560–567, 1909.

[23] R. A. Beth, "Mechanical detection and measurement of the angular momentum of light," *Physical Review*, vol. 50, no. 2, p. 115, 1936.

[24] N. Simpson, K. Dholakia, L. Allen, and M. Padgett, "Mechanical equivalence of spin and orbital angular momentum of light: an optical spanner," *Optics letters*, vol. 22, no. 1, pp. 52–54, 1997.

[25] K. Ladavac and D. G. Grier, "Microoptomechanical pumps assembled and driven by holographic optical vortex arrays," *Optics Express*, vol. 12, no. 6, pp. 1144–1149, 2004.

[26] J. H. Lee, G. Foo, E. G. Johnson, and G. A. Swartzlander Jr, "Experimental verification of an optical vortex coronagraph," *Physical review letters*, vol. 97, no. 5, p. 053901, 2006.

[27] A. Jesacher, S. Fürhapter, S. Bernet, and M. Ritsch-Marte, "Shadow effects in spiral phase contrast microscopy," *Physical review letters*, vol. 94, no. 23, p. 233902, 2005.

[28] G. Gibson, J. Courtial, M. Padgett, M. Vasnetsov, V. Pas' ko, S. Barnett, and S. Franke-Arnold, "Free-space information transfer using light beams carrying orbital angular momentum," *Optics Express*, vol. 12, no. 22, pp. 5448–5456, 2004.

[29] H. F. Schouten, G. Gbur, T. D. Visser, and E. Wolf, "Phase singularities of the coherence functions in young's interference pattern," *Optics letters*, vol. 28, no. 12, pp. 968–970, 2003.

[30] G. Gbur and T. D. Visser, "Coherence vortices in partially coherent beams," *Optics Communications*, vol. 222, no. 1, pp. 117–125, 2003.

[31] I. Freund, "Bichromatic optical lissajous fields," *Optics communications*, vol. 226, no. 1, pp. 351–376, 2003.

[32] G. V. Bogatyryova, C. V. Fel'de, P. V. Polyanskii, S. A. Ponomarenko, M. S. Soskin, and E. Wolf, "Partially coherent vortex beams with a separable phase," *Optics letters*, vol. 28, no. 11, pp. 878–880, 2003.

[33] D. Palacios, I. Maleev, A. Marathay, and G. Swartzlander Jr, "Spatial correlation singularity of a vortex field," *Physical review letters*, vol. 92, no. 14, p. 143905, 2004.

[34] G. Gbur and G. A. Swartzlander Jr, "Complete transverse representation of a correlation singularity of a partially coherent field," *JOSA B*, vol. 25, no. 9, pp. 1422–1429, 2008.

[35] S. Kim and G. Gbur, "Angular momentum conservation in partially coherent wave fields," *Physical Review A*, vol. 86, no. 4, p. 043814, 2012.

[36] M. Padgett, J. Arlt, N. Simpson, and L. Allen, "An experiment to observe the intensity and phase structure of laguerre–gaussian laser modes," *American Journal of Physics*, vol. 64, no. 1, pp. 77–82, 1996.

[37] M. Kristensen, M. Beijersbergen, and J. Woerdman, "Angular momentum and spin-orbit coupling for microwave photons," *Optics communications*, vol. 104, no. 4-6, pp. 229–233, 1994.

[38] N. Heckenberg, R. McDuff, C. Smith, and A. White, "Generation of optical phase singularities by computer-generated holograms," *Optics letters*, vol. 17, no. 3, pp. 221–223, 1992.

[39] G. Gbur, *Singular Optics*. Series in Optics and Optoelectronics, CRC Press, 2016.

[40] L. Mandel and E. Wolf, *Optical Coherence and Quantum Optics*. Cambridge University Press, 1995.

[41] E. Wolf, "New theory of partial coherence in the space–frequency domain. part i: spectra and cross spectra of steady-state sources," *JOSA*, vol. 72, no. 3, pp. 343–351, 1982.

[42] G. Gbur and T. D. Visser, "Phase singularities and coherence vortices in linear optical systems," *Optics communications*, vol. 259, no. 2, pp. 428–435, 2006.

[43] L. Mandel and E. Wolf, *Optical Coherence and Quantum Optics*. Cambridge U. Press, 1995.

[44] C. Stahl and G. Gbur, "Complete representation of a correlation singularity in a partially coherent beam," *Optics letters*, vol. 39, no. 20, pp. 5985–5988, 2014.

[45] C. Stahl and G. Gbur, "Partially coherent vortex beams of arbitrary order," *JOSA A*, vol. 34, no. 10, pp. 1793–1799, 2017.

[46] G. Gbur, T. D. Visser, and E. Wolf, "'Hidden' singularities in partially coherent wavefields," *Journal of Optics A: Pure and Applied Optics*, vol. 6, no. 5, p. S239, 2004.

[47] T. Wang, J.-x. Pu, and Z.-y. Chen, "Generation and propagation of partially coherent vortex beams," *Optoelectronics Letters*, vol. 5, no. 1, pp. 77–80, 2009.

[48] V. G. Shvedov, Y. V. Izdebskaya, A. V. Rode, A. Desyatnikov, W. Krolikowski, and Y. S. Kivshar, "Generation of optical bottle beams by incoherent white-light vortices," *Optics Express*, vol. 16, no. 25, pp. 20902–20907, 2008.

[49] G. Gbur and G. A. Swartzlander Jr, "Complete transverse representation of a correlation singularity of a partially coherent field," *JOSA B*, vol. 25, no. 9, pp. 1422–1429, 2008.

[50] J. Hass, M. Weir, and G. Thomas, *University Calculus*. Thomas Series, Pearson Addison-Wesley, 2007.

[51] G. Gbur and R. K. Tyson, "Vortex beam propagation through atmospheric turbulence and topological charge conservation," *JOSA A*, vol. 25, no. 1, pp. 225–230, 2008.

[52] L. Allen, M. W. Beijersbergen, R. Spreeuw, and J. Woerdman, "Orbital angular momentum of light and the transformation of Laguerre-Gaussian laser modes," *Physical Review A*, vol. 45, no. 11, p. 8185, 1992.

[53] G. A. Swartzlander Jr and R. I. Hernandez-Aranda, "Optical Rankine vortex and anomalous circulation of light," *Physical review letters*, vol. 99, no. 16, p. 163901, 2007.

[54] C. Stahl and G. Gbur, "Analytic calculation of vortex diffraction by a triangular aperture," *JOSA A*, vol. 33, no. 6, pp. 1175–1180, 2016.

[55] M. Vasnetsov, I. Marienko, and M. Soskin, "Self-reconstruction of an optical vortex," *Journal of Experimental and Theoretical Physics Letters*, vol. 71, no. 4, pp. 130–133, 2000.

[56] J. Hickmann, E. Fonseca, W. Soares, and S. Chávez-Cerda, "Unveiling a truncated optical lattice associated with a triangular aperture using light's orbital angular momentum," *Physical review letters*, vol. 105, no. 5, p. 053904, 2010.

[57] L. E. de Araujo and M. E. Anderson, "Measuring vortex charge with a triangular aperture," *Optics letters*, vol. 36, no. 6, pp. 787–789, 2011.

[58] M. E. Anderson, H. Bigman, L. E. de Araujo, and J. L. Chaloupka, "Measuring the topological charge of ultrabroadband, optical-vortex beams with a triangular aperture," *JOSA B*, vol. 29, no. 8, pp. 1968–1976, 2012.

[59] A. Mourka, J. Baumgartl, C. Shanor, K. Dholakia, and E. M. Wright, "Visualization of the birth of an optical vortex using diffraction from a triangular aperture," *Optics express*, vol. 19, no. 7, pp. 5760–5771, 2011.

[60] J. B. Keller, "Geometrical theory of diffraction," *JOSA*, vol. 52, no. 2, pp. 116–130, 1962.

[61] A. B. Thidés, L. Palmieris, and C. G. Somedas, "Encoding many channels on the same frequency through radio vorticity: first experimental test," *New Journal of Physics. Pdf-tiedosto. Saatavissa: http://iopscience. iop. org/1367-2630/14/3/033001/pdf/1367-2630_ 14_ 3_ 033001. pdf. Luettu*, vol. 26, p. 2015, 2012.

[62] J. Wang, J.-Y. Yang, I. M. Fazal, N. Ahmed, Y. Yan, H. Huang, Y. Ren, Y. Yue, S. Dolinar, M. Tur, *et al.*, "Terabit free-space data transmission employing orbital angular momentum multiplexing," *Nature Photonics*, vol. 6, no. 7, pp. 488–496, 2012.

[63] M. Krenn, R. Fickler, M. Fink, J. Handsteiner, M. Malik, T. Scheidl, R. Ursin, and A. Zeilinger, "Communication with spatially modulated light through turbulent air across vienna," *New Journal of Physics*, vol. 16, no. 11, p. 113028, 2014.

[64] A. Wheelon, "Electromagnetic scintillation, vol. 1," *One: Geometrical Optics*, 2001.

[65] L. C. Andrews, R. L. Phillips, and C. Y. Hopen, *Laser beam scintillation with applications*, vol. 99. SPIE press, 2001.

[66] D. L. Knepp, "Multiple phase-screen calculation of the temporal behavior of stochastic waves," *Proceedings of the IEEE*, vol. 71, no. 6, pp. 722–737, 1983.

[67] J. Martin and S. M. Flatté, "Intensity images and statistics from numerical simulation of wave propagation in 3-d random media," *Applied Optics*, vol. 27, no. 11, pp. 2111–2126, 1988.

[68] V. Maarten, J. H. Le Rousseau, and R.-S. Wu, "Generalization of the phase-screen approximation for the scattering of acoustic waves," *Wave Motion*, vol. 31, no. 1, pp. 43–70, 2000.

[69] W. Cheng, J. W. Haus, and Q. Zhan, "Propagation of vector vortex beams through a turbulent atmosphere," *Optics express*, vol. 17, no. 20, pp. 17829–17836, 2009.

APPENDIX A: PENTAGONAL APERTURE

Below is the table of parameterization coefficients for a pentagon. In the table,

$$h = \frac{1}{2}\tan\left(\frac{3}{10}\pi\right) \tag{A.1}$$

$$L = \sqrt{h^2 + \left(\frac{1}{2}\right)^2} \tag{A.2}$$

$$b = L\sin\left(\frac{1}{10}\pi\right) \tag{A.3}$$

$$\nu = \cos\left(\frac{4}{10}\pi\right) \tag{A.4}$$

Table A.1: Coefficients of Parameterization for Each Side of a Pentagon

Side	$\boldsymbol{\alpha_x}$	$\boldsymbol{\beta_x}$	$\boldsymbol{\alpha_y}$	$\boldsymbol{\beta_y}$
1	1	0	0	$-h$
2	ν	$1/2 + \nu/2$	$b + h$	$-h/2 + b/2$
3	$-1/2 - \nu$	$1/4 + \nu/2$	$L - b$	$b/2 + L/2$
4	$-1/2 - \nu$	$-1/4 - \nu/2$	$b - L$	$b/2 + L/2$
5	ν	$-1 + \nu$	$-b - h$	$b/2 - h/2$

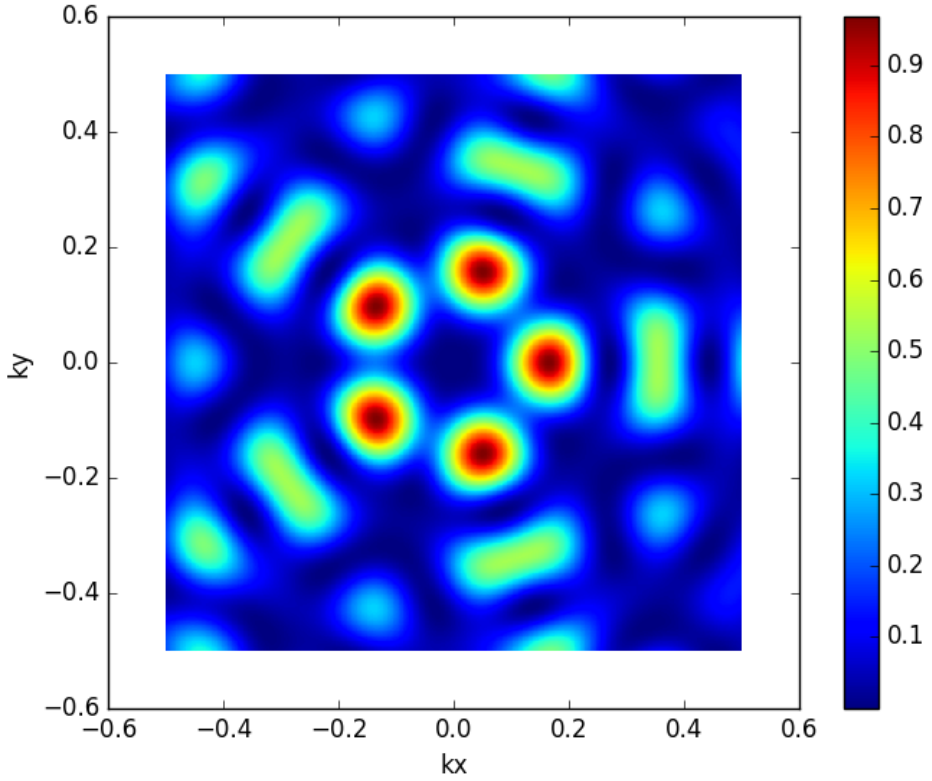

Figure A.1: On-axis diffraction pattern of a LGVB through a pentagonal aperture. $a = 4\lambda$, $w_0 = 2a$.